physchem

MDPI

Article

Multi-Target Computational Analysis of Monacolin X Against Angiogenesis-Associated Receptors

Vennila Jayaraman [1,†], Madan Kumar Arumugam [1,*], Sirpu Natesh Nagabhishek [1,†], Shana Balachandran [1], Jayaprakash Jayaraman [1], Chandru Nandhagopal [1], Muruganantham Bharathi [2,3] and Thiyagarajan Gopal [4]

[1] Cancer Biology Lab, Centre for Molecular and Nanomedical Sciences, Sathyabama Institute of Science and Technology, Chennai 600119, Tamil Nadu, India; venni.nila54@gmail.com (V.J.); nagabhishek.nat@gmail.com (S.N.N.); shanabalachandran@gmail.com (S.B.); jayaprakashjbt@nct.ac.in (J.J.); chandruchand910@gmail.com (C.N.)
[2] Centre for Bioinformatics, Karpagam Academy of Higher Education, Coimbatore 641021, Tamil Nadu, India; drbharathim89@gmail.com
[3] Department of Biochemistry, Karpagam Academy of Higher Education, Coimbatore 641021, Tamil Nadu, India
[4] Centre for Laboratory Animal Technology and Research, Sathyabama Institute of Science and Technology, Chennai 600119, Tamil Nadu, India; mailthiyagarajang@gmail.com
* Correspondence: madankumarbio@gmail.com or madankumar@sathyabama.ac.in
† These authors contributed equally to this work.

Abstract

Breast cancer (BC) is a serious global health problem with increasing incidence and mortality, while current treatments are often associated with severe side effects and drug resistance. Therefore, new therapeutic agents with enhanced efficacy and minimal adverse effects are needed. Our previous study reported the anti-angiogenic effect of Monacolin X, a secondary metabolite of a marine-sponge-associated fungus, using combined in vitro, ex vivo, in vivo (including a DMBA-induced mammary carcinoma rat model) and in silico approaches, identifying VEGFR2 as its principal target. In this study, molecular docking and molecular dynamics (MD) simulations were performed to investigate the interactions between Monacolin X and key anti-angiogenic targets, including IGFR, EGFR, neuropilin 1 (NRP1), Tie-2, VEGFR1/2, and PDGFRα, using Schrödinger Glide XP. Selective inhibitors were used for comparison. Docking analysis showed significant binding affinities of Monacolin X toward IGFR (G-score = −9.05), PDGFRα (−7.57), VEGFR1 (−7.42), Tie-2 (−7.40), VEGFR2 (−7.515), EGFR (−6.80), and NRP1 (−5.15), with hydrogen bonding, hydrophobic contacts, and electrostatic interactions contributing to stable complexes. Notably, IGFR and Tie-2 exhibited strong interactions, suggesting potential inhibition of angiogenic signaling. MD simulations were performed for 50 ns at 300 K and 1 bar; complex stability was assessed using RMSD and RMSF analyses, and the persistence of key active site hydrogen bonds was quantified as a percentage of simulation frames. MM-PBSA binding free-energy calculations further supported the thermodynamic feasibility of these interactions. Overall, these findings highlight Monacolin X's potential as an anti-angiogenic agent for BC. However, further in vitro and in vivo studies are required to validate its efficacy and clinical relevance.

Keywords: Monacolin X; anti-angiogenesis; molecular docking; molecular dynamics; IGFR; EGFR; neuropilin; Tie; VEGFR1; VEGFR2; PDGFR

Academic Editor: Tsuyoshi Michinobu

Received: 5 September 2026
Revised: 15 October 2026
Accepted: 21 October 2026
Published: 25 October 2026

Copyright: © 2026 by the authors. Licensee MDPI, Basel, Switzerland. This article is an open access article distributed under the terms and conditions of the Creative Commons Attribution (CC BY) license.

1. Introduction

Breast cancer (BC) is one of the most commonly diagnosed malignancies and a leading cause of cancer-related mortality among women worldwide [1]. BC ranks second among all types of cancer, with an incidence rate of 2,434,087 new cases, and ranks fourth with a mortality rate of 693,660 cases globally. In 2024, Asia accounted for the highest breast cancer incidence (IR) with an increased mortality rate (MR) (IR = 1,096,973; MR = 334,713 cases), followed by Europe (IR = 542,140 cases; MR = 140,198 cases), North America (IR = 320,723 cases; MR = 51,775 cases), Africa (IR = 225,643 cases; MR = 100,070 cases), Latin America and the Caribbean (IR = 218,121 cases; MR = 61,565 cases), and Oceania (IR = 30,487 cases; MR = 5339 cases). In Asia, China ranked first in IR (375,808 cases), and India ranked first for increased MR (96,100 cases) due to BC [2]. This poses a global health challenge, with significant regional disparities in incidence, mortality, and survival outcomes [3,4]. Tumor-induced angiogenesis is integral to tumor growth and plays a pivotal role in BC cells' survival, growth, invasion, and metastasis [5]. In this context, the key angiogenic receptors, insulin-like growth factor receptor 1 (IGFR) [6,7], epidermal growth factor receptor (EGFR) [8], vascular endothelial growth factor receptors (VEGFRs) [9], platelet-derived growth factor receptor (PDGFR) [10], neuropilin (NRP1) [11], and Tie-2 receptor (TIE2) [12], have been implicated in sprouting new blood vessels and causing therapeutic resistance in BC.

Anti-IGFR antibodies, like ganitumab, failed in phase III clinical trials due to adverse effects that include hyperglycemia, metabolic syndrome, and higher levels of growth hormone. Therefore, effective anti-IGFR-targeted therapy is urgently needed to inhibit IGFR signaling and prevent BC progression and metastasis [13,14]. EGFR-targeted tyrosine kinase inhibitors (TKIs), including pyrotinib and vandetinib, likely address intrinsic resistance because EGFR mutations occur more frequently. This suggests that higher-generation TKIs are needed to target and prevent progression of EGFR-associated BC [15,16]. Meanwhile, NRP1 interacts with VEGFR2 and directs signaling toward angiogenesis, and no FDA-approved drugs directly target NRP1. However, drugs that target VEGFR2, including bevacizumab, could indirectly affect the function of NRP1 [9]. Similarly, no drugs are available that directly inhibit PDGFR to treat BC. However, avapritinib could target the PDGFR D842V mutation and inhibit the progression of gastrointestinal stromal tumors [17]. These studies suggested the need to identify novel, safer therapeutic agents to treat BC.

In recent years, natural products have emerged as promising clinical candidates, including taxanes, vinca alkaloids, camptothecins, podophyllotoxin derivatives, epipodophyllotoxins, homoharringtonine, and artemisinin and its derivatives [18]. Endo et al. originally reported Monacolin X in 1985 as a metabolite isolated from a mutant *Monascus ruber* culture. It was described as structurally similar to monacolin K and was investigated for inhibition of cholesterol biosynthesis/HMG-CoA reductase [19]. Our previous study reported the isolation and characterization of Monacolin X from *Monascus sp.* NMK7, a fungus associated with the marine sponge *Clathria frondifera*. Monacolin X exhibited anticancer activity against breast cancer cell lines, including MCF-7, T47D, MDA-MB-231, and MDA-MB-468 [20]. Furthermore, our study demonstrated the anti-angiogenic potential of Monacolin X through the downregulation of VEGFR2 signaling, as evaluated using in vitro (HUVEC), ex vivo (aortic ring), in vivo (CAM assay, zebrafish, and DMBA-induced mammary carcinoma in rats), and in silico approaches [20]. Monacolin X has also shown potential for hepatocellular carcinoma treatment [21] and may inhibit angiogenesis through interactions with the Cys919 residue of VEGFR2. However, its potential to target angiogenic pathways by including IGFR, EGFR, NRP, TIE receptors, VEGFR1/2, and PDGFR in breast cancer has not been thoroughly investigated using a multi-dimensional approach that includes in silico, in vitro, and in vivo methods to understand the exact

https://doi.org/10.3390/physchem6040064

mechanisms of Monacolin X in inhibiting the angiogenesis process to treat BC. Therefore, this study used an in silico approach to assess the anti-angiogenic potential of Monacolin X against the targets IGFR, EGFR, NRP, TIE receptors, VEGFR1/2, and PDGFR.

2. Results

2.1. Molecular Docking Studies of Monacolin X Against the Selected Targets VEGFR1, TIE2, EGFR, IGFR, NRP1, PDGFRα, and VEGFR2

Monacolin X was docked against the selected targets (VEGFR1, TIE2, EGFR, IGFR, NRP1, PDGFRα, and VEGFR2), and its interaction feasibility was compared with that of their synthetic inhibitors across all targets (Figures 1A–D–14A–D). The symbols used in the interaction diagrams (Figures 1–14) are as follows: purple/magenta arrows denote hydrogen bonds (solid arrows in the docking panels A; dashed arrows with a percentage in the post-simulation panels B); green lines denote π–π stacking; red lines denote π–cation interactions; grey spheres labeled H_2O denote water molecules mediating a bridged hydrogen bond; and residue bubbles are colored by residue type (green, hydrophobic; light blue, polar; red, acidic; dark blue/violet, basic). The percentage beside a contact in panel B is its contact occupancy over the 50 ns trajectory.

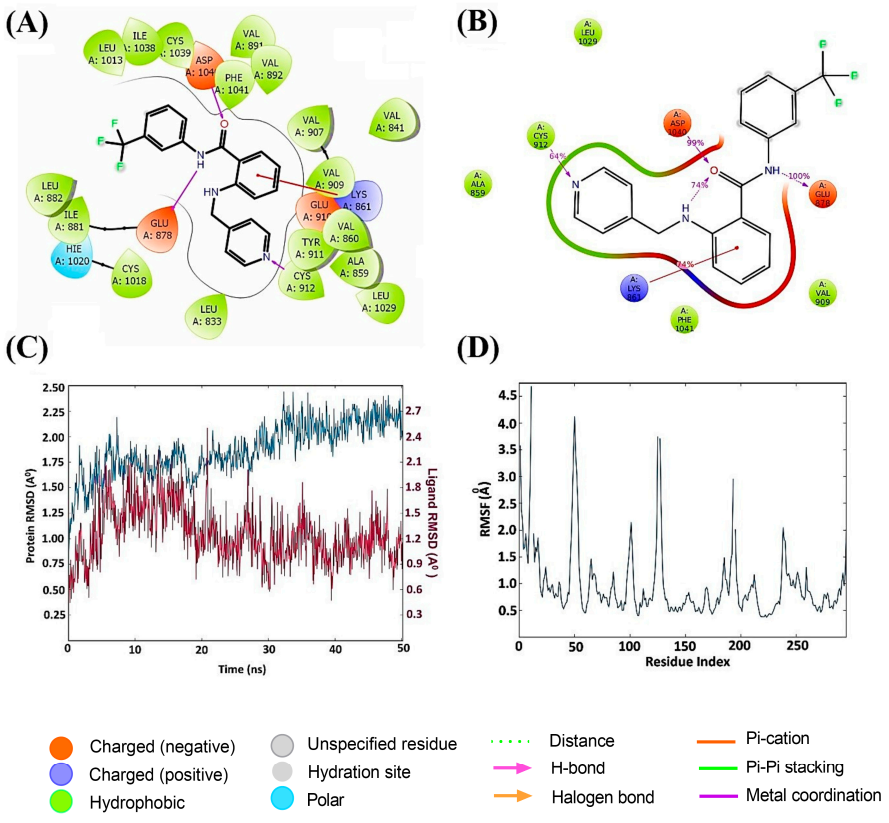


Figure 1. Docking and molecular dynamics simulation results of the VEGFR-1-AAL-993 complex. (**A**). Binding profiles of AAL-993 at the end of docking studies. (**B**). Binding profiles of AAL-993 at the end of simulations. (**C**). Deviations made by the receptor in the presence of AAL-993 during 50 ns of simulation. (**D**). Fluctuations in the receptor amino acids during simulations.

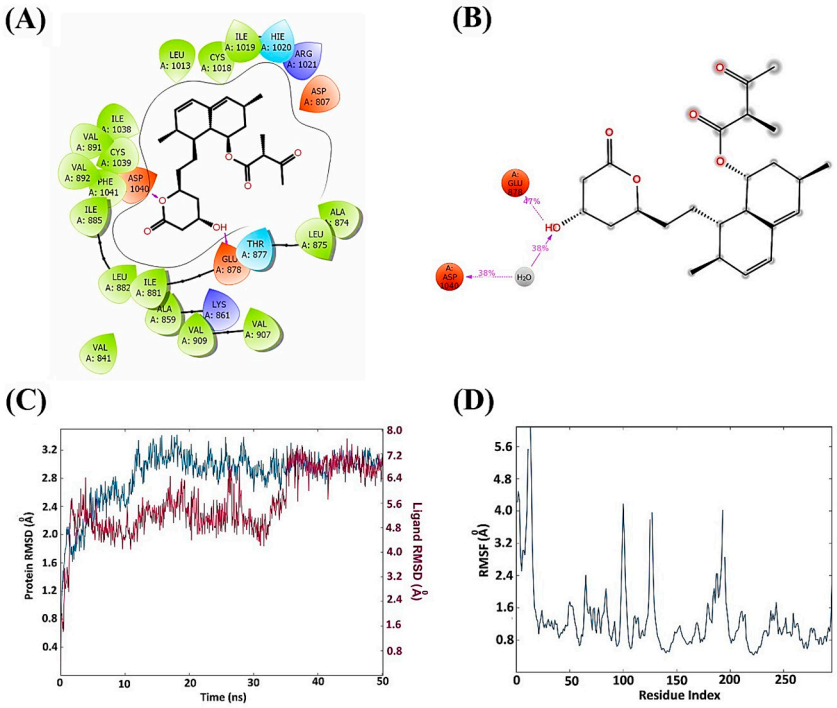


Figure 2. Docking and molecular dynamics simulation results of the VEGFR-1–Monacolin X complex. (**A**). Binding profiles of Monacolin X at the end of docking studies. (**B**). Binding profiles of Monacolin X at the end of simulations. (**C**). Deviations made by the receptor in the presence of Monacolin X during 50 ns of simulation. (**D**). Fluctuations in the receptor amino acids during simulations.

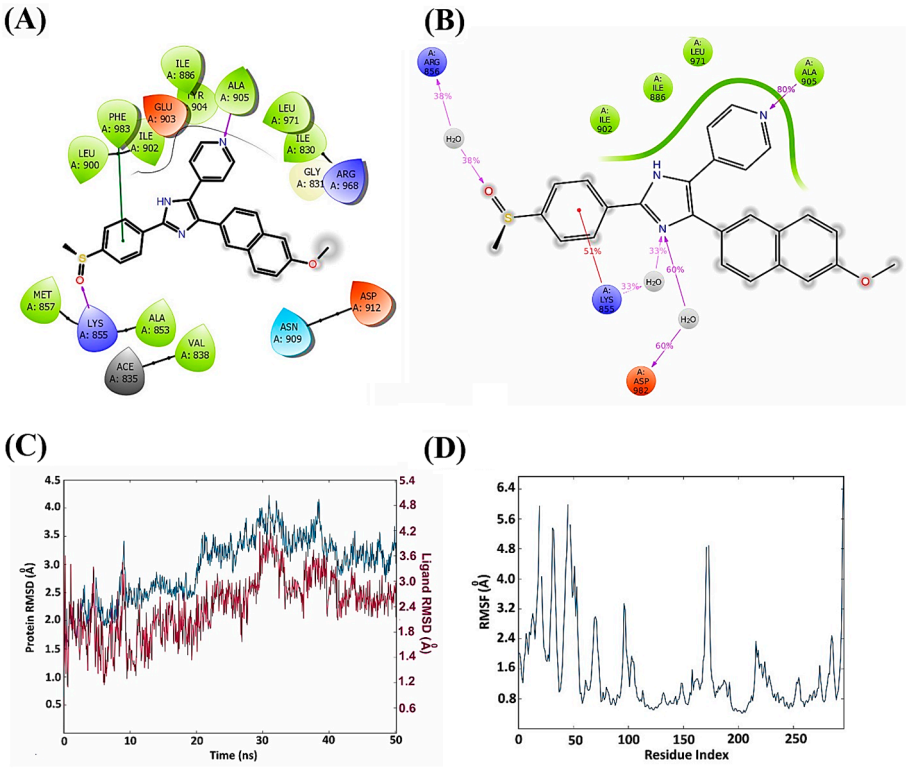


Figure 3. Docking and molecular dynamics simulation results of the SB-203580-TIE2 receptor complex. (**A**). Binding profiles of SB-203580 at the end of docking studies. (**B**). Binding profiles of SB-203580 at the end of simulations. (**C**). Deviations made by the receptor in the presence of SB-203580 during 50 ns of simulation time. (**D**). Fluctuations in the receptor amino acids during simulations.

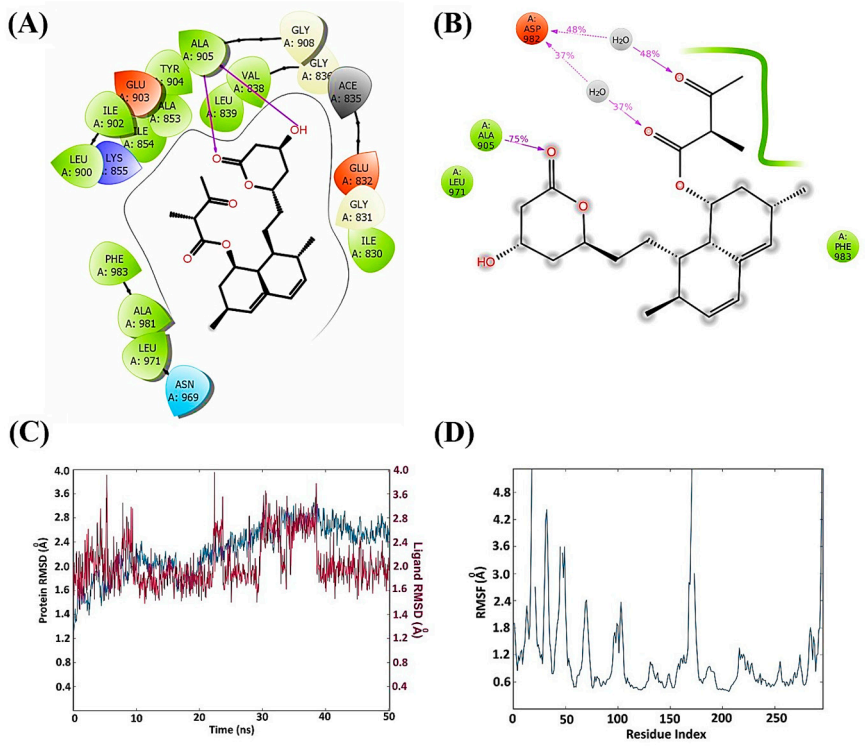


Figure 4. Docking and molecular dynamics simulation results of Monacolin X–TIE2 receptor complexes: (**A**). Binding profiles of Monacolin X at the end of docking studies. (**B**). Binding profiles of Monacolin X at the end of simulations. (**C**). Deviations made by the receptor in the presence of Monacolin X during 50 ns of simulation time. (**D**). Fluctuations in the receptor amino acids during simulations.

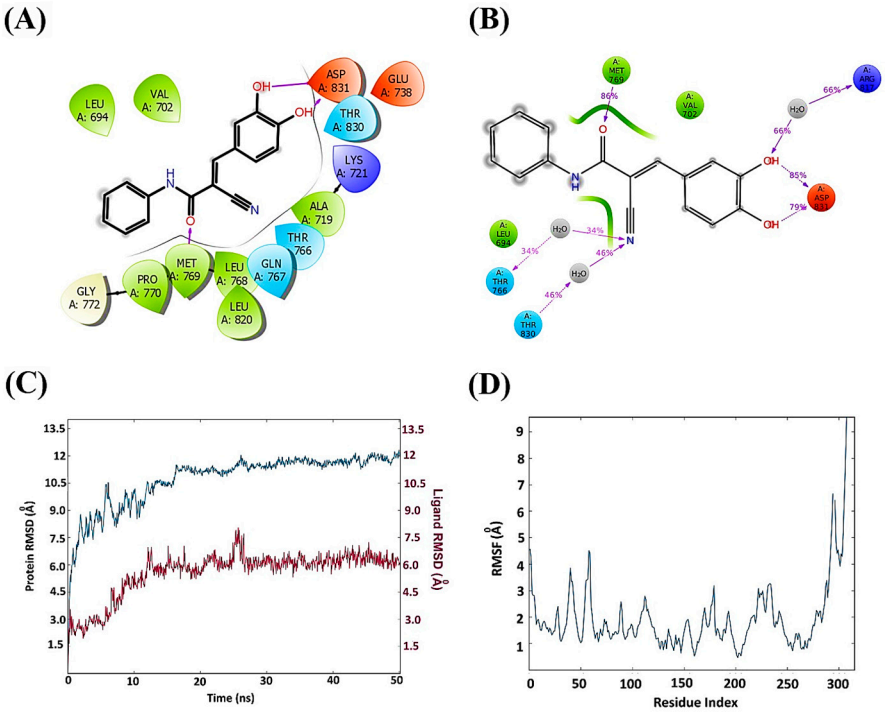


Figure 5. Docking and molecular dynamics simulation results for receptor complexes: (**A**). Binding profiles of AG494 at the end of docking studies. (**B**). Binding profiles of AG494 at the end of simulations. (**C**). Deviations of the receptor in the presence of AG494 over 50 ns of simulation time. (**D**). Fluctuations in the receptor amino acids during simulations.

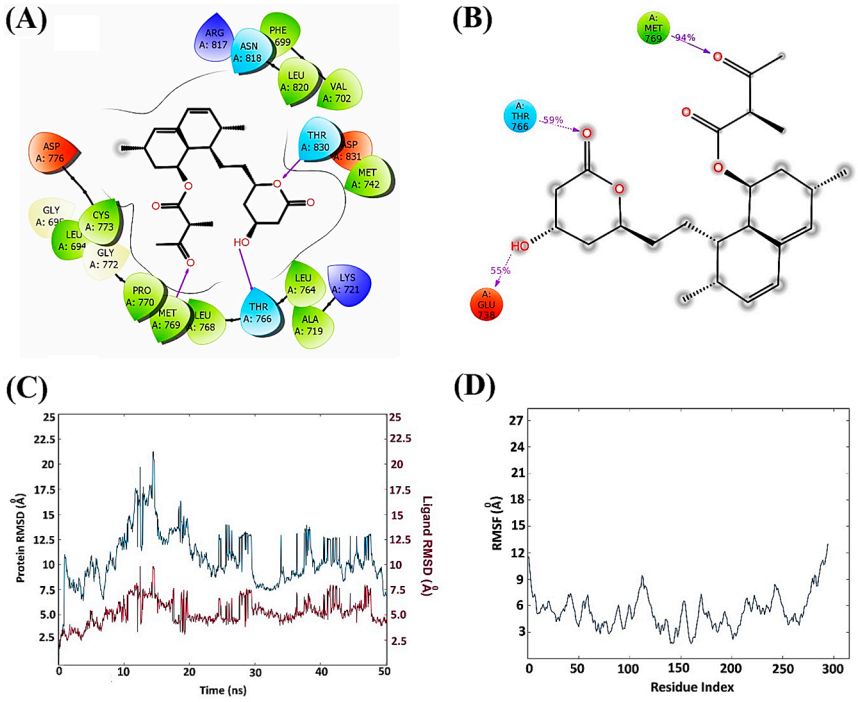


Figure 6. Docking and molecular dynamics simulation results of Monacolin X–EGFR receptor complexes. (**A**). Binding profiles of Monacolin X at the end of docking studies. (**B**). Binding profiles of Monacolin X at the end of simulations. (**C**). Deviations made by the receptor in the presence of Monacolin X during 50 ns of simulation time. (**D**). Fluctuations in the receptor amino acids during simulations.

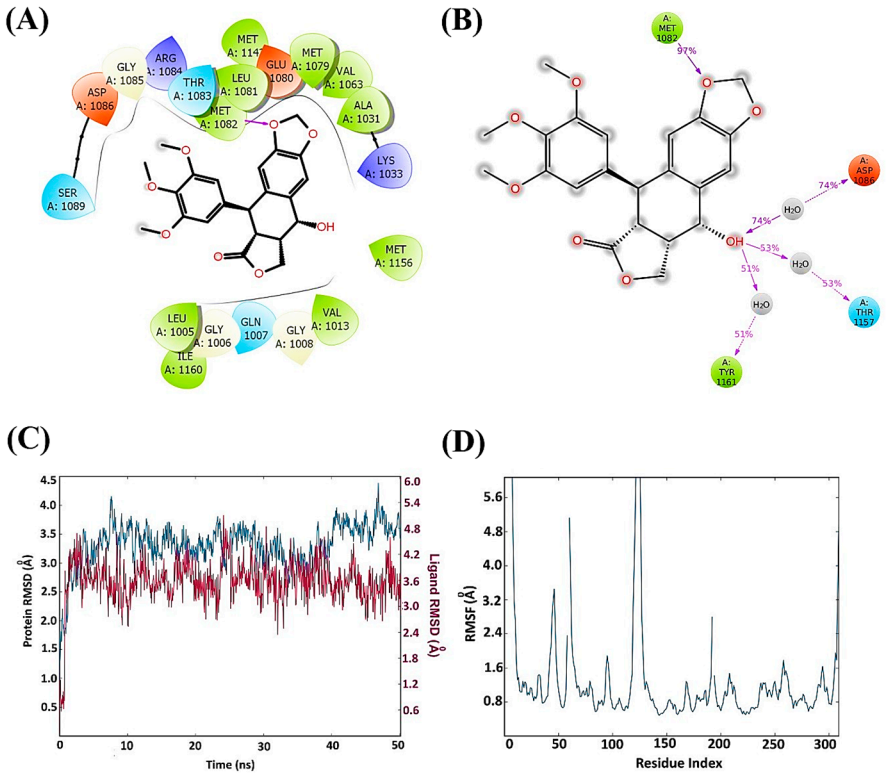


Figure 7. Docking and molecular dynamics simulation results of PQ401-IGFR receptor complexes. (**A**). Binding profiles of PQ401 at the end of docking studies. (**B**). Binding profiles of PQ401 at the end of simulations. (**C**). Deviations made by the receptor in the presence of PQ401 during 50 ns of simulation time. (**D**). Fluctuations in the receptor amino acids during simulations.

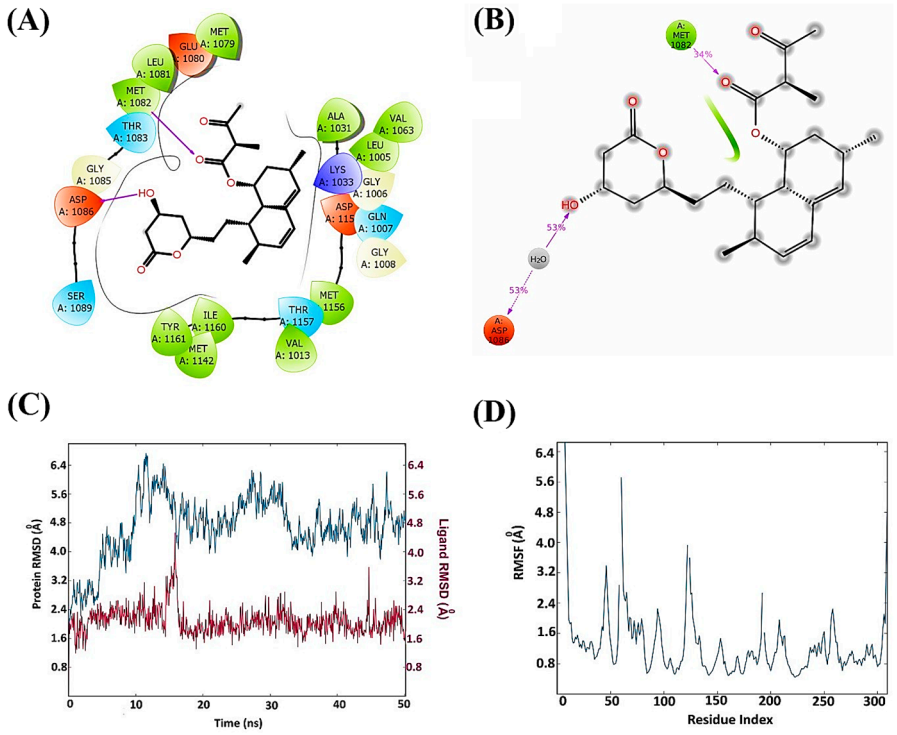


Figure 8. Docking and molecular dynamics simulation results of Monacolin X–IGFR complexes. (**A**). Binding profiles of Monacolin X at the end of docking studies. (**B**). Binding profiles of Monacolin X at the end of simulations. (**C**). Deviations made by the receptor in the presence of Monacolin X during 50 ns of simulation time. (**D**). Fluctuations in the receptor amino acids during simulations.

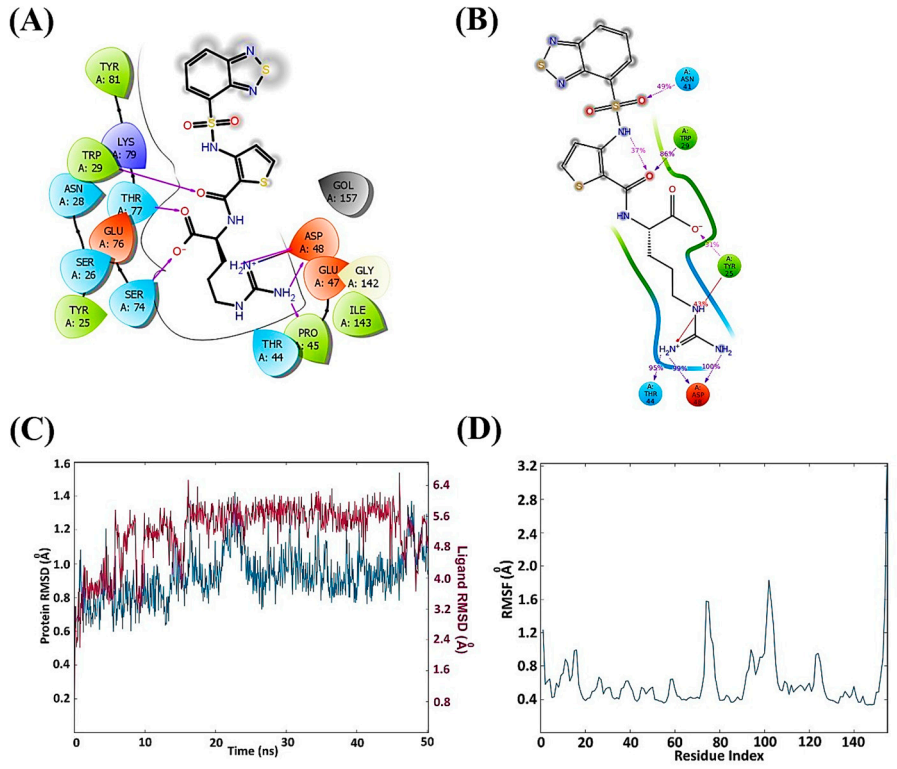


Figure 9. Docking and molecular dynamics simulation results of EG00229-NRP1 receptor complexes. (**A**). Binding profiles of EG00229 at the end of docking studies. (**B**). Binding profiles of EG00229 at the end of simulations. (**C**). Deviations made by the receptor in the presence of EG00229 during 50 ns of simulation time. (**D**). Fluctuations in the receptor amino acids during simulations.

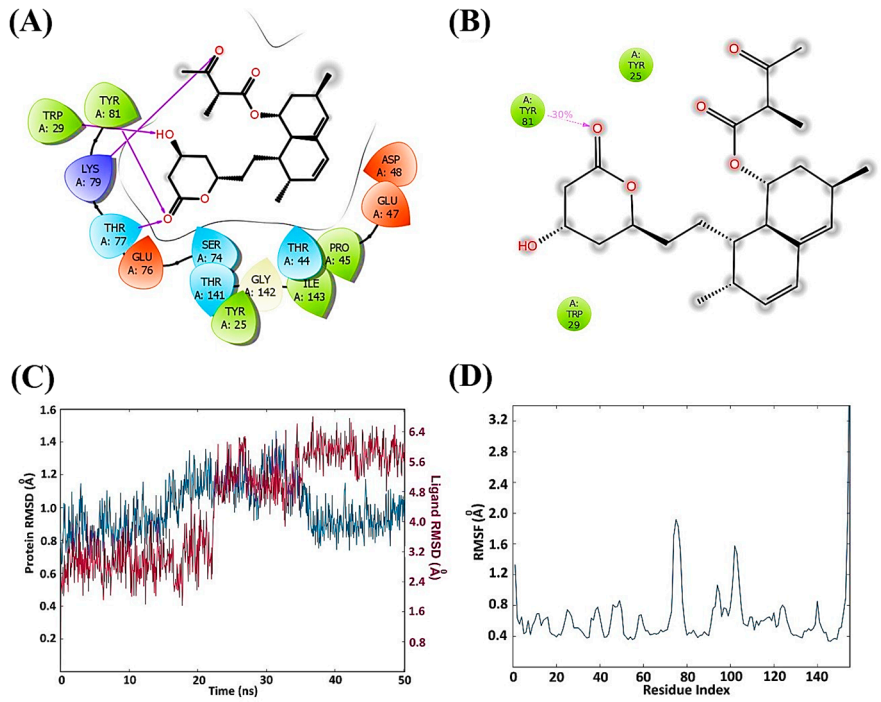


Figure 10. Docking and molecular dynamics simulation results of Monacolin X–NRP1 receptor complexes. (**A**). Binding profiles of Monacolin X at the end of docking studies (**B**). Binding profiles of Monacolin X at the end of simulations. (**C**). Deviations made by the receptor in the presence of Monacolin X during 50 ns of simulation time. (**D**). Fluctuations in the receptor amino acids during simulations.

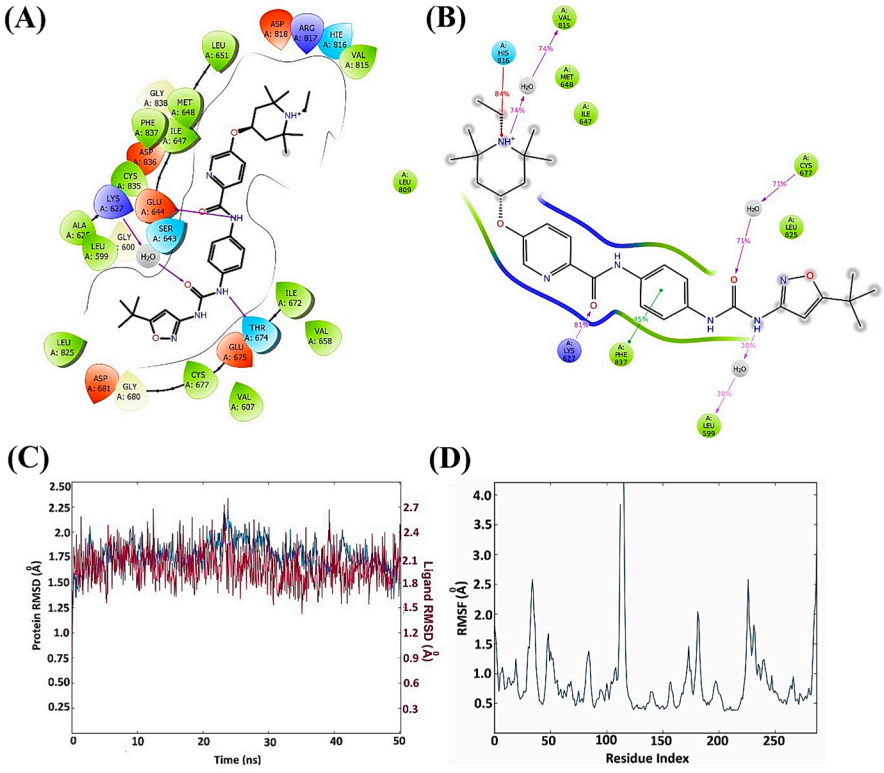


Figure 11. Docking and molecular dynamics simulation results of AC710-PDGFRα receptor complexes. (**A**). Binding profiles of AC710 by the end of docking studies. (**B**). Binding profiles of AC710 at the end of the simulations. (**C**). Deviations made by the receptor in the presence of AC710 during 50 ns of simulation time. (**D**). Fluctuations in the receptor amino acids during simulations.

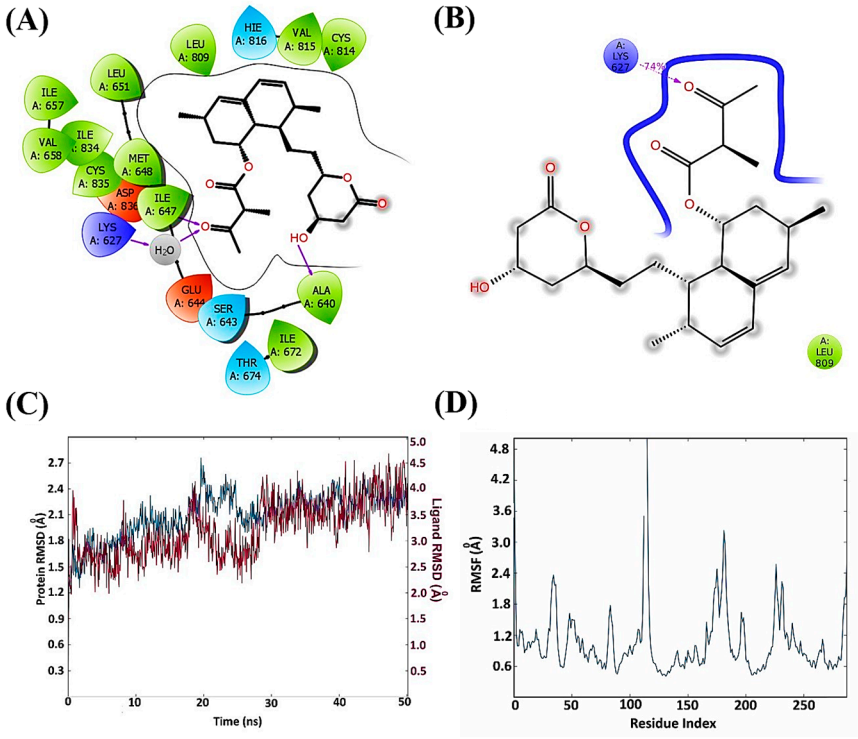


Figure 12. Docking and molecular dynamics simulation results of Monacolin X–PDGFR*α* complexes. (**A**). Binding profiles of Monacolin X at the end of docking studies. (**B**). Binding profiles of Monacolin X at the end of simulations. (**C**). Deviations made by the receptor in the presence of Monacolin X during 50 ns of simulation time. (**D**). Fluctuations in the receptor amino acids during simulations.

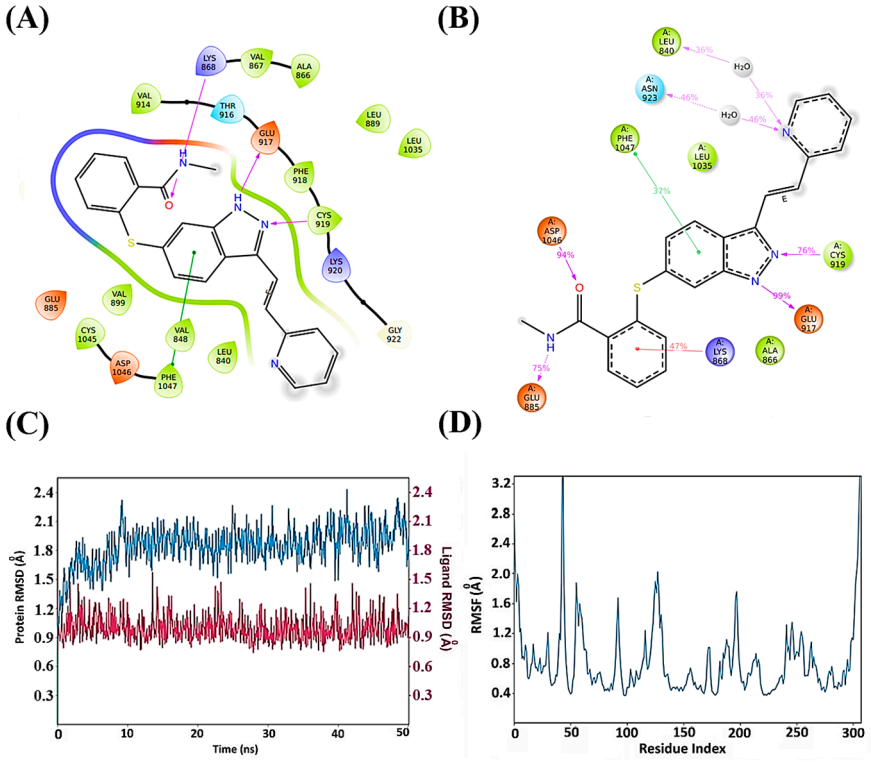


Figure 13. Docking and molecular dynamics simulation results of Axitinib–VEGFR2 complexes. (**A**). Binding profiles of Axitinib at the end of docking studies. (**B**). Binding profiles of Axitinib at the end of simulations. (**C**). Deviations made by VEGFR2 in the presence of Axitinib during 50 ns of simulation time. (**D**). Fluctuations in VEGFR2 amino acids during simulations.

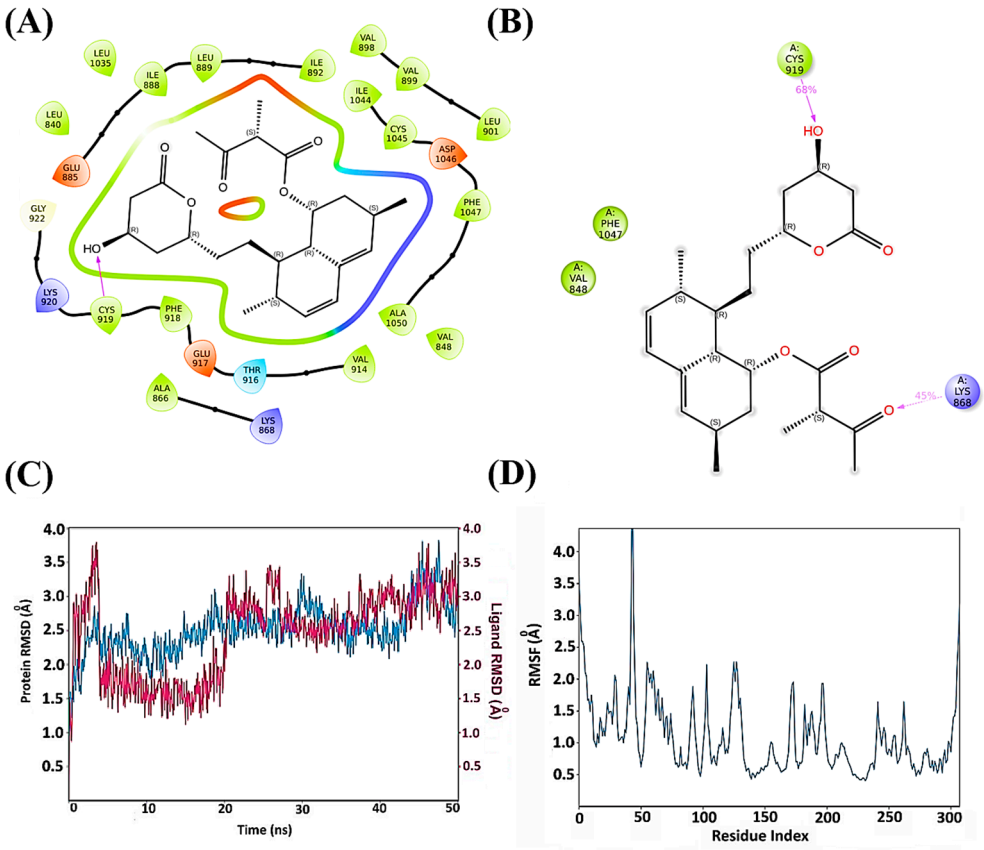


Figure 14. Docking and molecular dynamics simulation results of Monacolin X–VEGFR2 complexes. (**A**). Binding profiles of Monacolin X at the end of docking studies (**B**). Binding profiles of Monacolin X at the end of simulations (**C**). Deviations made by VEGFR2 in the presence of Monacolin X during 50 ns of simulation time. (**D**). Fluctuations in VEGFR2 amino acids during simulations.

2.2. Interaction Profiles of AAL-993 and Monacolin X with VEGFR1

VEGFR1 was prepared using the Protein Preparation Wizard, and its active site was defined using the Receptor Grid Generation tool. The SiteMap analysis revealed that a major portion of the active pocket is composed of hydrophobic amino acids, including Ala874, Leu875, Ala859, Ile881, Leu882, Ile885, Val891, Val892, Val907, Val909, Leu1013, Cys1018, Ile1019, Ile1038, Cys1039, and Phe1041. Previous reports indicate that key active site residues, such as Asp1040 and Glu878, engage in hydrogen bond interactions with known inhibitors. In previous reports, key active site residues such as Asp1040 and Glu878 were involved in hydrogen bond interactions with known inhibitors.

The synthetic VEGFR1 inhibitor, AAL-993, interacted with Glu878 (oxygen atom) with the NH group, Asp1040 (NH) with =O, and Cys912 (NH) with the nitrogen atom of the inhibitor via hydrogen bonds. The complex displayed a pi–cation interaction with Lys861 and had a G-score of −12.28 (Figure 1A,B). These complexes were further refined using molecular dynamics simulations, during which protein–ligand stability was evaluated by analyzing structural deviations, residue fluctuations, and interaction profiles. The synthetic drug-like molecule AAL-993 retained all interactions observed during the docking studies. The deviations of AAL-993 in the presence of the VEGFR1 active site were low, ranging from 0.5 to 1.8 Å. Initially, it started at 0.5 Å, reached a maximum around 18 ns, thereafter declined and settled around 1.0–1.5 Å. The majority of residues in the protein exhibited fluctuations below 1.0 Å, while a few residues, primarily located in loop regions, showed higher fluctuations exceeding 2.5 Å (Figure 1C,D).

The docking study of Monacolin X with the VEGFR1 binding site revealed two hydrogen bond interactions: Asp1040 (NH) with the oxygen atom of Monacolin X and

Glu878 (oxygen atom) with the OH group, with a G-score of −7.42 (Figure 2A). However, Monacolin X failed to maintain contact with Asp1040 and retained interaction with Glu878 (Figure 2B). In the VEGFR1–Monacolin X complex, protein deviations started at 1.0 Å, increased to a maximum of 3.2 Å at the end of 11 ns, and thereafter stabilized around 2.8–3.2 Å. By the end of 1 ns, Monacolin X reached 5.5 Å and maintained a deviation range of 4.8–5.6 Å between 2 and 35 ns. At 35 ns, a sudden jump in deviations from 5.6 Å to 7.2 Å was observed, and the pace remained at around 7.2 Å until the end of the simulation run (Figure 2C,D).

2.3. Interaction Profiles of SB-203580 with TIE2

The TIE2 receptor was retrieved from the PDB and prepared using the Protein Preparation Wizard. The prepared ligands were then docked into the receptor's active site. Important receptor active site residues were noted as follows: Ala 905, Tyr 904, Glu 903, Ile 902, Phe 983, Leu 900, Met 857, Lys 855, Ala 853, Leu 971, Ile 830, Gly 831, Asn 909, Asp 912, and Arg 968. In the docking studies, SB-203580 interacted well with Ala 905 and Lys 855 via hydrogen bonds and with Phe 983 via a pi–cation interaction. The hydrogen bond interaction profiles showed Ala 905 (NH) with the nitrogen (N) atom and Lys 855 (NH) with the =O attached to the sulfur atom of SB-203580. The complex after docking exhibited a G-score of −8.66 (Figure 3A).

The trajectory files obtained from the 50 ns simulation run were used to analyze the binding interactions between the TIE2 receptor and the ligands SB-203580 and Monacolin X based on deviations and fluctuations.

The simulation interaction diagram of the TIE2 receptor with the standard drug SB-203580 showed one hydrogen bond with Ala 905 and one pi–cation stacking with Lys 855 (Figure 3B). The hydrogen bond with Ala 905 observed during the docking studies was retained after the simulation studies with the same nitrogen atom of the standard drug molecule. Also, the TIE2 receptor deviations were observed from 0.8 Å to 3.0 Å. However, more deviations were observed between 30–35 ns and 38–40 ns (Figure 3C). Meanwhile, fluctuations in the TIE2 receptor amino acids were observed mainly between residues 0–50 and 170–180 (Figure 3D).

Upon advancing to the Monacolin X-TIE2 receptor complex, the molecule also formed an important hydrogen bond interaction with Ala 905. The molecule formed two hydrogen bond interactions between the OH and =O atoms attached to the same six-membered ring in Monacolin X and the =O and NH groups of the Ala 905 residue, with a G-score of −7.40 (Figure 4A). The second hydrogen bond with Lys855 observed after docking was converted to pi–cation stacking during the simulation, and the remaining interaction with Phe 983 disappeared by the end of the simulation. However, the crucial interaction of Ala905 was retained after the simulation studies. In the case of Monacolin X, the interaction with Ala905 was retained in the simulation studies via a single hydrogen bond, whereas the docking studies showed two hydrogen bonds (Figure 4B). Deviations of the protein and ligand during the simulation were within almost the same range, with similar inclination and declination in the deviation peaks. The deviations of Monacolin X in the TIE2 receptor active site were predominantly centered around 2.4 Å throughout the simulation. Noticeable increases in deviation were observed during the time intervals of 0–10 ns, 21–23 ns, and 30–40 ns. However, for the majority of the simulation period, the deviations remained stable at approximately 2.4 Å. In contrast, the TIE2 receptor exhibited deviations ranging from 1.6 to 3.2 Å over the 50 ns simulation. Across the entire trajectory, the receptor displayed periodic fluctuations, indicating consistent structural adjustments in the presence of Monacolin X. Residue-level fluctuations were generally maintained below 2.5 Å, with only a few prominent peaks observed (Figure 4C,D).

2.4. Interaction Profiles of AG494 and Monacolin X with EGFR

The standard drug AG494-EGFR complex interacted via three hydrogen bonds. In this, the two OH groups of AG494 shared two bonds with Asp 831 (oxygen atom, =O), and the third bond was shared by the NH of Met 769 with the =O of the inhibitor, yielding a G-score of −7.0 (Figure 5A). The binding profiles of the two complexes were analyzed after the simulation studies to identify whether they were maintained during the simulation studies. AG494 in complex with EGFR retained the interactions observed during the docking studies throughout the simulation period. The interaction profiles made by residues Asp 831 and Met 769 with the inhibitor were similar in both the docking and simulation studies (Figure 5B). Interestingly, the complex, after the molecular dynamics simulations, shows deviations in scale for both the protein and the ligand. Protein deviations were reported between 3.0 and 12 Å, and ligand deviations were recorded between 3.0 and 6.0 Å. The deviations reported were very high compared to the normal acceptable range (2.0–3.0 Å). In the complex, both the receptor and the standard inhibitor maintained stable deviation graphs throughout the simulation (Figure 5C). Even with inclined deviations, receptor residues maintained fluctuations below 2.5 Å, and tail-end residues showed inclinations; tail-end fluctuation graph inclinations were noted as a common feature in the simulations (Figure 5D).

The molecule of interest, Monacolin X, maintained three hydrogen contacts with residues in the receptor's active site, with a G-score of −6.8. The three hydrogen bond interaction profiles were: Met 769(NH) with =O; Thr 830(OH) with an oxygen atom; and Thr 766 (oxygen atom) with the OH group of Monacolin X (Figure 6A). In the Monacolin X interaction profile with EGFR from the simulation studies, the molecule was reported to form three hydrogen bonds with residues in the receptor's active site. The residues participating in the interaction profile were Glu 738, Met 769, and Thr 766. Comparing the docking and simulation interaction profiles, Met 769 and Thr 766 were retained, and the Thr 830 interaction observed during docking studies was lost. A new H-bond interaction formed with Glu 738 during simulation studies (Figure 6B).

The H-bond interaction profile of Met 769 remained the same in both studies (Figures 5B and 6B). In contrast, the Thr 766 interaction shifted to the =O group in the same ring, previously with the OH group, and a new Glu 738 interaction was observed at this position. This complex also exhibited huge deviations during the simulation run. The EGFR deviations in Monacolin X are much higher than those of the complex EGFR-AG494. The EGFR deviations were observed in the range 2.5–21 Å, and Monacolin X deviations were graphed between 2.5 and 5.0 Å, with frequent inclinations up to 9.0 Å (Figure 6C). Throughout the entire simulation run time, both EGFR and Monacolin X exhibited similar inclination and declination indices. When EGFR deviations increased, Monacolin X deviations in the same phase also increased, and similar declination patterns were observed. EGFR residual fluctuations were high, and the range was between 2 and 13 Å. Residues with the largest fluctuations were observed in the tail-end regions, and most fluctuations were between 3 and 9 Å (Figure 6D).

2.5. Interaction Profiles of PQ401 and Monacolin X with IGFR

Two ligands, the standard inhibitor and Monacolin X, were docked into the active site of IGFR using Glide extra precision docking procedures. IGFR interacted well with the standard inhibitor PQ401, forming hydrogen bonds with Met 1082, a crucial residue in IGFR inhibition studies, yielding a G-score of −7.86. The hydrogen bond was shared between Met 1082 (NH) and the oxygen atom of PQ401. Other interactions, such as salt bridges and stacking, were absent in this IGFR-PQ401 complex (Figure 7A). Both molecules fit well inside the binding pocket of IGFR during simulation studies and retained important interactions. At the end of the simulation studies, both the standard inhibitor

and PQ401 retained interactions with the Met 1082 residue in the active site of IGFR (Figure 7B).

Deviations of IGFR in the IGFR-PQ401 complex were reported as 1.0–4.0 Å. Initially, receptor deviations were high. By nearly 10 ns, they stabilized around 3.0–3.5 Å and continued with small inclinations and declinations up to 40 ns; at the end of the simulations, deviations were noted between 3.5 and 4.0 Å. PQ401 deviations initially ranged around 0.5 Å and then suddenly shifted to 3.6 Å over a 1 ns period. Later, the majority of deviations were reported in the range of 3.0 to 4.0 Å (Figure 7C). Referring to fluctuations in the residues in IGFR, in complex with the standard inhibitor PQ401, during the simulation studies, they were below 1.6 Å, which is considered an acceptable range. Some residues within the structure showed high fluctuations due to their locations near gaps and in loops. The tail-end residues' natural tendency to produce high fluctuations was also observed in this IGFR-PQ401 complex (Figure 7D).

A similar type of Met 1082 interaction was also observed in the Monacolin X–receptor complex. Similarly, another interaction was observed with the residue Asp 1086 (=O), which formed a hydrogen bond with the OH group of Monacolin X, and the complex had a G-score of −9.05 (Figure 8A). However, Monacolin X lost the hydrogen bond interaction with Asp 1086 by the end of the simulation (Figure 8B). IGFR in complex with Monacolin X showed higher inclination and declination throughout the simulation period. The minimum deviation of IGFR was 2.0 Å, reported at the start of the simulation; the maximum deviation was 6.5 Å, reported at 11 ns; and the average deviation was 4.0–5.5 Å. Monacolin X produced deviations inside the active site of the receptor during simulations (1.6–4.5 Å). Maximum ligand deviations were observed in only one instance, around 17 ns into the simulation run, and most deviations were between 1.6 and 2.4 Å (Figure 8C). Receptor residual fluctuations are almost similar to the receptor–standard inhibitor complex, with the majority of fluctuations below 1.6 Å (Figure 8D).

2.6. Interaction Profiles of EG00229 and Monacolin X with NRP1

The standard inhibitor EG00229 formed five hydrogen bonds, one pi–pi stacking interaction, and a salt bridge with the active site of NRP1. Of the five hydrogen bonds, two were shared with Asp 48 (=O and oxygen atom), and the remainder were shared with NH2 and NH2+ of the inhibitor, Ser 74 with the oxygen atom, and Thr 77 (OH) with =O of the inhibitor molecule. The remaining inhibitor molecule interactions were a salt bridge with Asp 48 (Figure 9A). The interactions between the standard inhibitor EG00229 and NRP1, as determined by the simulation studies, were maintained by three hydrogen bonds and a pi–cation interaction. The EG00229 molecule formed two hydrogen bonds with Asp 48; one hydrogen bond was with Tyr 25, and a pi–cation interaction was also observed with the same residue. Additionally, three H-bond interactions with Trp 29, Asn 41, and Thr 44 were observed for the inhibitor in the simulation studies (Figure 9B). The G-score of EG00229 with the NRP1 complex was identified as −5.40.

The NRP1 deviations in complex with the standard inhibitor EG00229 were observed between 0.6 and 1.4 Å. During the simulations, NRP1 maintained an increasing deviation range over the time scale. Similarly, EG00229 deviations were also in an incremental state up to 18 ns; later, stable deviations were observed around 5.6 Å until 45 ns, and the last 5 ns were reported with up-and-down deviations around 4.0–5.6Å (Figure 9C). During the simulations, the residues' fluctuations were reported to be below 2.0 Å, with the majority below 0.8 Å (Figure 9D).

The Monacolin X–NRP1 complex formed four H-bond interactions with a G-score of −5.15, and interactions made by Monacolin X with active site residues were the oxygen atom with Trp 29 (NH), =O with Thr 77 (OH), =O with Lys 79 (NH), and =O with Tyr 81 (OH) (Figure 10A). However, Monacolin X retained only one hydrogen bond with Tyr 81

after the simulation studies, compared with the four hydrogen bonds observed during the docking studies (Figure 10B).

The deviations of NRP1 with Monacolin X were observed in the range of 0.7–1.4 Å (Figure 10C), similar to those in the NRP1-EG00229 complex (Figure 9C). At 31 ns, the deviations were within an acceptable range and declined from 40 ns to 0.8–1.0 Å. In contrast to NRP1 deviations, Monacolin X deviations were in a stable state up to 22 ns, noted around 2.8–3.2 Å, and at the end of the 50 ns simulation time, deviations were found to be in an increasing phase. The Monacolin X deviations ranged from 2.4 to 6.4 Å (Figure 10C).

2.7. Interaction Profiles of AC710 and Monacolin X with PGDFRα

AC710 interacted well with PGDFRα via hydrogen bonds with the residues GLU644 (NH) and THR674 (NH), and a water-mediated hydrogen bond with LYS627, exhibiting a G-score of −5.56 (Figure 11A). Interestingly, the water-mediated hydrogen bond with the residue Lys 627 was converted into a direct hydrogen bond with the AC170 inhibitor at the end of the simulation. Likely, another water-mediated hydrogen bond with AC170 is formed by the residues Leu 599, Cys 677, and Val 815 (Figure 11B). Deviations in the protein and ligand of PGDFRα–AC170 were reported to be acceptable throughout the simulation period. Receptor deviations were between 1.5 and 2.5 Å. During the simulation interval of 20–27 ns, the minimum inclination was observed, then decreased to 2.1 Å and finally reached 2.3 Å at the end of the run (Figure 11C). During the simulation, fluctuations in amino acids in the PDGFRα-AC170 complex were reported to be below 2.4 Å, except in two regions, around 110–120 and 170–180 amino acids (Figure 11D).

Monacolin X (=O and OH) formed two hydrogen bonds, one with Asp 836 (=O) and the other with Ala 640 (=OH), as indicated by a G-score of −7.57 (Figure 12A). At the end of the simulations, the inhibitor formed an interaction with Leu 809 and a new hydrogen bond with Lys 627, rather than the hydrogen bond that was observed in the docking studies (Figure 12B).

Similarly, PDGFRα in complex with AC170 showed deviations from 1.5 to 2.3 Å, and only a sudden inclination occurred between 20 and 27 ns, which are also in the acceptable range. Likely, Monacolin X also showed deviations ranging from 1.2 Å to 4.5 Å. Interestingly, Monacolin X has declination deviations during the 20–27 ns period, which contrasts with protein deviations at this particular time frame (Figure 12C). The receptor deviations range from 1.5 to 2.0 Å, and the standard inhibitor range is 1.8–2.4 Å. The majority of the receptor amino acids fluctuated below 1.25 Å. Fluctuations above 2.5 Å were observed between 110 and 120 amino acids (Figure 12D).

2.8. Interaction Profiles of Axitinib and Monacolin X with VEGFR2

Axitinib and VEGFR2 interacted via hydrogen bonds with the residues Lys 868 (=O), Glu 917 (=NH), and Cys 919 (=N), and the G-score was estimated at −9.678 (Figure 13A). Interestingly, the observed hydrogen bonds with the residues Glu 917 (=N) and Cys 919 (=N) were retained, and new hydrogen bonds formed at the end of the simulation, including Glu 885 (=NH) and Asp 1046 (=O). Also, water-mediated hydrogen bonds were formed with the residues Asn 923 and Leu 840 (Figure 13B). Deviations of VEGFR2 with regard to the complex VEGFR2–Axitinib were acceptable throughout the simulation time period. The VEGFR2 deviations were recorded as 0.10–2.1 Å. Meanwhile, Monacolin X reported deviations between 0.9 and 0.9 Å with a minimal inclination up to 1.5 Å (Figure 13C). Fluctuations in VEGFR2 residues were recorded as 1.6–2.0 Å, except for the residues at positions 43 and 45, which include Ala 860 and Thr 861. These fluctuating residues are not involved in hydrogen bond formation (Figure 13D).

Similarly, Monacolin X interacted with VEGFR2 via only one hydrogen bond with the residue Cys 919 (=OH), and the G-score was estimated as −7.515 (Figure 14A). Even

though only one hydrogen bond formed with Monacolin X, it was retained throughout the simulation period, and an additional hydrogen bond was formed at the end of the simulation with the residue Lys 868 (=O) (Figure 14B).

The deviations of VEGFR2 in the VEGFR2–Monacolin X complex were recorded at 1.5–2.5 Å from 0 to 19 ns; after that, they increased and then settled again after 20–30 ns; then, another increase was observed, reaching up to 3.8 Å. The Monacolin X deviations were recorded between 1.0 and 3.5 Å, except for 5–6 and 45–47 ns, which were recorded above 3.5 Å (Figure 14C). Meanwhile, the VEGFR2 amino acid fluctuations were recorded approximately between 1.0 and 2.3 Å, except for the residues positioned at 42 and 43, which were identified as Asp 857 and Ala 860 (Figure 14D). The overall results of molecular docking and dynamics, including the G-score, H-bond residues in docking, H-bonds retained during the MD simulations via direct and water-mediated binding with the occupancy percentage (%) for the complex Monacolin X, were evaluated using VEGFR1, TIE2, EGFR, IGFR, NRP1, PGDFRα, and VEGFR2 and are presented in Table 1.

Table 1. Selected angiogenesis-associated targets and their interactions with reference inhibitors and Monacolin X based on molecular docking and molecular dynamics analyses.

Target (PDB)	Ligand	G-Score (Kcal/mol)	H-Bond Residues in Docking	H-Bond Retained During the MD	
				Direct Interactions (Occupancy, %)	Water-Mediated Interactions (Occupancy, %)
VEGFR1 (3HNG)	AAL-993	−12.28	GLU878, GLU912, ASP1042	CYS912 (64%), GLU878 (100%), ASP1040 (99%)	-
	Monacolin X	−7.42	GLU878, ASP1040	GLU878 (47%)	ASP1040 (38%)
TIE2 (2WQB)	SB-203580	−8.66	LYS855, ALA905	ALA905 (80%)	LYS855 (33%), ARG856 (38%), ASP982 (60%)
	Monacolin X	−7.40	ALA905 (2)	ALA905 (75%)	ASP982 (2) (48% and 37%)
EGFR (1M17)	AG494	−7.0	MET769, ASP831 (2)	MET769 (86%), ASP831 (2) (85% and 79%)	THR766 (34%), ARG817 (66%), THR830 (46%)
	Monacolin X	−6.8	THR766, MET769, THR830	GLU738 (55%), THR766 (59%), MET769 (94%)	-
IGFR (5FXQ)	PQ401	−7.86	MET1082	MET1082 (97%)	ASP1086 (74%), THR1157 (53%), TYR1161 (51%)
	Monacolin X	−9.05	MET1082, ASP1086	MET1082 (34%)	ASP1086 (53%)
NRP1 (3I97)	EG00229	−5.40	TRP29, PRO45, GLU47, ASP48, SER74, THR77	TYR25 (31%), TRP29 (86%), ASN41 (49%), THR44 (95%), ASP48 (2: 100%, 99%)	-
	Monacolin X	−5.15	TRP29, THR77, LYS79, TYR81	TYR81 (30%)	-
PGDFRα (5GRN)	AC710	−5.56	GLU644, THR674	LYS627 (81%)	LEU599 (38%), CYS677 (71%), VAL815 (74%)
	Monacolin X	−7.57	ALA640, ILE647	LYS627 (74%)	-
VEGFR2 (3U6J)	Axitinib	−9.678	LYS868, GLU917, CYS919	GLU885 (75%), GLU917 (99%), CYS919 (76%), ASP1046 (94%)	LEU840 (36%), ASN923 (46%)
	Monacolin X	−7.515	CYS919	LYS868 (45%), CYS919 (68%)	-

https://doi.org/10.3390/physchem6040064

3. Discussion

Angiogenesis is a critical driver of breast cancer progression, supporting tumor growth, invasion, and metastatic dissemination through coordinated receptor tyrosine kinase-mediated signaling, including IGFR [22], EGFR [23], VEGFR1/2 [24,25], TIE2 receptor [12,26], and PDGFR [27], together with the angiogenic co-receptor NRP1, a member of non-tyrosine kinase cell surface glycoproteins [11,28]. Despite the availability of targeted therapies, each treatment faces fundamental constraints, with clinical outcomes remaining limited due to drug resistance, off-target toxicity, and pathway redundancy [29–31].

Consequently, multi-target-directed small molecule inhibitors, a concept known as polypharmacology, particularly those derived from natural sources, are increasingly being explored as alternative therapeutic strategies with improved safety profiles [32–34]. In this context, the present study systematically evaluates Monacolin X as a multi-target anti-angiogenic agent by comparing it with the standard drugs for each of the mentioned angiogenic targets, using a standard in silico framework.

The results of molecular docking and simulation studies showed that the standard molecule formed significant interactions with the VEGFR1 residues, including Asp1040 (99%), Glu878 (100%), and Cys912 (64%) residues in the active site, which are known to be critical for kinase inhibition and ligand stabilization [35,36]. In contrast, Monacolin x interacted only with two residues of VEGFR1, such as Asp1040 (99%) and Glu878 (100%), via hydrogen bonds. However, it retained interactions with these residues, interacting directly and via water with Glu878 (47%) and Asp1040 (38%). Deviations in VEGFR1 in the Monacolin x complex were higher than in the AAL-993 complex (Figures 1 and 2A–D). These results indicate that the standard inhibitor AAL-993 interacted well with the VEGFR1 active site, as discussed earlier. Therefore, based on our results, Monacolin exhibited minimal activity against VEGFR1 compared to AAL-993.

Interaction with the TIE2 receptor, particularly the important catalytic core residue Ala 905, was observed in both complexes [37]. The percentage of interaction varies between the standard inhibitor SB-203580 (80%) and Monacolin X (75%), as observed in simulation studies. SB-203580 exhibited a stronger binding affinity (G-score: −8.66 kcal/mol) than Monacolin X (−7.40 kcal/mol), which is expected given its role as a standard inhibitor. It interacts with Ala 905 via a hydrogen bond and with Lys 855 via a π–cation interaction, suggesting a stable interaction within the catalytic pocket of the TIE2 receptor. These interactions highlight the importance of hydrogen bonding and electrostatic interactions in stabilizing TIE2 receptor–SB-203580 complexes (Figure 3A,B). However, Monacolin X also interacted well with the TIE2 receptor by forming dual hydrogen bonds with Ala 905. In this, one hydrogen bond to this residue was maintained throughout the simulation. The persistence of this key interaction highlights the structural relevance of Ala 905 in Monacolin stabilization (Figure 4A,B). Meanwhile, simulation results further confirmed the stability of both complexes. In this, SB-203580 exhibited fluctuations observed between 30 and 40 ns, suggesting transient conformational adjustments within the receptor that may correspond to ligand-induced structural rearrangements (Figure 3C). Alternatively, Monacolin X exhibited stable interactions with the TIE2 receptor, reaching equilibrium after initial adaptation phases, with deviations predominantly centered around ~2.5 Å (Figure 4C). Also, residue-level fluctuation analysis revealed that most amino acids fluctuated within acceptable flexibility and did not destabilize the TIE2 receptor structure (Figures 3D and 4D). These findings suggest that Monacolin X may inhibit TIE2 receptor-mediated angiogenesis.

The standard drug AG494 interacted well with EGFR, which exhibits a G-score of −7.0. In this, three hydrogen bonds formed with the residues Asp 831 (2), i.e., 85% and 79%, and Met 769 (86%) in docking studies; these interactions were retained even after

simulation, and new water-mediated hydrogen bonds were formed with the residues Thr 766, Arg 817, and Thr 830 (Figure 5A,B). However, EGFR exhibited greater structural deviation during the simulation, and the standard drug AG494 also deviated substantially, exceeding the ≤3.0 Å limit and reaching up to 12 Å. Meanwhile, the residues also fluctuated significantly, as reflected by elevated RMSF values (Figure 5C,D). Similarly, Monacolin X interacted with EGFR by forming three hydrogen bonds with residues Thr766, Met769, and Thr830, which are key residues of the ATP-binding pocket essential for ligand recognition and stabilization. These residues lie in the hinge region and play a crucial role in the interactions of the lead compound Erlotinib, a well-known EGFR inhibitor [38], by facilitating key hydrogen bond interactions that stabilize ATP-competitive ligands. During the simulation, it retained key interactions with Thr766 (59%) and Met769 (94%), while an additional hydrogen bond was observed with Glu738 (55%). However, Monacolin X failed to fully replicate the interaction profile of the standard inhibitor AG494, with only partial overlap in binding interactions (Figure 6A,B). Furthermore, Monacolin X exhibited a higher RMSD of 2.3–5.0 Å, with a maximum inclination of 21 Å and RMSF values observed between 9 and 12 Å, indicating increased structural deviations and residue-level fluctuations (Figure 6C,D). These findings indicate that substantial conformational deviations occurred for both EGFR complexes interacting with AG94 and Monacolin X. During the simulation, persistent hydrogen bond interactions were observed, indicating that specific ligand–protein contacts were maintained throughout. However, the relatively high RMSD and RMSF values warrant cautious interpretation of the overall structural stability.

The docking results for IGFR-PQ401 and Monacolin X, based on G-scores, suggest that Monacolin X is superior to the standard inhibitor. Interestingly, PQ401 and Monacolin formed a hydrogen bond interaction with the crucial residue Met 1082, which plays a significant role in ligand-binding mechanisms, even after simulation [39]. The percentage of hydrogen bond formation for the standard inhibitor (97%) was higher than that of Monacolin X (34%). This suggests that the standard inhibitor formed a H-bond with Met 1082 throughout the simulation, whereas Monacolin X's interaction with the residue was partial (Figures 7A,B and 8A,B). However, the Monacolin X deviations (2.4–2.4 Å except 13–15 ns) and fluctuations are lower when compared with the standard drug (Figures 7C,D and 8C,D). Therefore, based on these observations, Monacolin X could act as a partial inhibitor of IGFR, relative to a known inhibitor.

Interestingly, during docking and simulations, the inhibitor molecule EG00229 made five hydrogen bonds with the residues in the active site of NRP1. One more change observed after simulation concerning the standard inhibitor was the conversion of pi–pi stacking to pi–cation interactions, with residual interaction percentages at Asp 48 (99 and 100%), Thr 44 (95%), Tyr 25 (31%), Trp 29 (86%), and Asn 41 (49%). Alternatively, Monacolin X retained only the Tyr 81 (30%) interaction when compared to the standard drug interaction percentage profile. Based on docking and simulation results, EG00229 was more potent than Monacolin X in producing inhibitory activity against NRP1, even though the RMSD and RMSF were more similar to each other (Figures 9A–D and 10A–D).

The PDGFRα-AC710 complex was more stable than the Monacolin X complex based on the projected deviations observed during simulations. Compared to the binding efficiency standard inhibitor interaction percentage with the common residue Lys 627 (81%), it was higher than that of Monacolin X (74%). Also, the supporting residual interactions observed in the standard receptor complex were not established in the Monacolin X complex (Figures 11A–D and 12A–D).

Several studies have reported Cys 919, Asp 1046, and Glu 885 as important amino acids in the VEGFR2 binding pocket [20]. To act as an effective inhibitor, the ligand must show predominant interactions, especially with Cys 919, a crucial amino acid among the

three reported. The present in silico study focused on the interactions between Monacolin X and key amino acids during docking and molecular dynamics simulations. Axitinib, a well-known reported active inhibitor, was chosen for a comparative study in the work design. Docking studies provided insight into the accommodation of two molecules within the VEGFR2 active site and their interactions. In the docking study, two molecules successfully formed a hydrogen bond with the Cys 919 residue. Also, at the end of the simulation run, both molecules retained the hydrogen bond interaction with the crucial amino acid Cys 919. Axitinib and Monacolin X showed hydrogen bond interactions with Cys 919 (76% and 68%, respectively). The flexibility between the receptor and ligand facilitates the generation of conformers, and during conformational changes, the two molecules interact with Cys 919, thereby stabilizing the complex. The Cys 919 residue of the receptor was found to form a strong H-bond (94%) with the =N group of the molecule because of minimal torsions in single bonds attached to that particular benzene ring (Figures 13A–D and 14A–D).

Overall, the comparative molecular docking and molecular dynamics analyses demonstrated that Monacolin X interacted with seven angiogenesis-associated targets, although the strength and persistence of these interactions varied across the investigated proteins. Monacolin X exhibited the most favorable docking score against IGFR (G-score = −9.05 kcal/mol); however, the interaction with the key Met1082 residue was maintained for only 34% of the simulation, together with a water-mediated interaction with Asp1086 observed for 53% of the trajectory. In comparison, Monacolin X showed a less favorable docking score against VEGFR2 (G-score = −7.515 kcal/mol) but retained a hydrogen bond interaction with the important Cys919 residue for 68% of the simulation. Persistent interactions were also observed with key residues of TIE2 (G-score = −7.40 kcal/mol), which include ALA905 and ASP982 (2) with the interaction percentages of 75%, 48%, and 37%, and PDGFRα (G-score = −7.57 kcal/mol), which includes LYS627 with the interaction percentage of 74%, whereas the interaction profile of VEGFR1–Monacolin X (G-score = −7.42 kcal/mol) exhibits only two water-mediated hydrogen bonds with the residues GLU878 and ASP1040, with interaction percentages of 47% and 38%, respectively. Monacolin X showed three direct hydrogen bonds with the residues GLU738, THR766, and MET769 of EGFR (G-score = −6.8 kcal/mol), with interaction percentages of 55%, 59%, and 94%, and NRP1–Monacolin X (G-score = −5.15 kcal/mol) showed one hydrogen bond with TYR81, with an interaction percentage of 30%. These findings demonstrate that docking scores alone do not fully reflect the persistence of ligand–target interactions during molecular dynamics simulations and that both predicted binding and interaction stability should be considered when evaluating potential target engagement. Importantly, the persistent interaction between Monacolin X and VEGFR2 Cys919 is consistent with our previous in vitro evidence of its VEGFR2-associated activity. Collectively, while the present computational findings support a broader interaction profile of Monacolin X with angiogenesis-associated targets, the combined docking, molecular dynamics, and previous experimental evidence provide particular support for VEGFR2 as a biologically relevant candidate target of Monacolin X in breast cancer angiogenesis.

4. Methodology

4.1. Protein Preparation

The target proteins were selected based on their well-established roles in angiogenic and vasculogenic signaling in BC progression and stage advancement. VEGFR1 and VEGFR2, also known as FLT1 and KDR, are well-known predominant targets in angiogenic signaling, especially in interaction with VEGF [40,41]. Angiopoietin promotes angiogenesis and vascular sprouting via the TIE2 receptor when VEGF is upregulated in the extracellular matrix [42]. Aberrant EGFR signaling likely contributes to BC progression

and angiogenesis by triggering downstream pathways such as MAPK, PI3K/AKT, STAT, and PLCγ/PKC [43,44]. IGF1R likely activates the PI3K/AKT pathway, which primarily controls cell proliferation, differentiation, and vasculogenesis [45,46]. Similarly, NRP1 is a unique transmembrane glycoprotein and non-tyrosine kinase co-receptor that interacts with multiple ligands, modulating various signaling pathways and triggering angiogenesis in tumor conditions [28]. Also, PDGFRα signaling contributes to angiogenesis and immune modulation [47]. Hence, we selected these proteins as targets. The 3-D structures for VEGFR2 (PDB ID: 3U6J) [48], VEGFR1 (PDB ID: 3HNG) [49], TIE2 (PDB ID: 2WQB) [50], EGFR (PDB ID: 1M17) [51], IGFR (PDB ID: 5FXQ) [52], NRP1 (PDB ID: 3I97) [53] and PDGFRα (PDB ID: 5GRN) [54] were retrieved from the PDB. The protein preparation wizard was used to prepare the receptors, zero-order bonds to metal atoms, bond orders to hydrogen, selenomethionine-to-methionine reconversion, and capping of the termini. Surrounding the co-crystallized ligand, free water molecules beyond 5 Å were removed from the protein, preserving the water-mediated interactions and the protein binding site's native environment; at pH 7.0, tautomeric/ionization states were generated for the ligand. Furthermore, to resolve overlapping hydrogen bonds, the protein's hydrogen bonding network was optimized. Finally, the protein structure was energetically minimized using the OPLS-2005 force field derived from the Optimized Potentials for Liquid Simulations (OPLS) framework [55]. The potential ligand-binding pockets of the prepared proteins were predicted using the SiteMap module of the Schrödinger Suite. Based on the SiteMap analysis, the binding pocket corresponding to the co-crystallized ligand was identified and selected for subsequent docking studies. Grid boxes were then generated for the receptors around the selected binding pocket, with the grid center defined based on the position of the co-crystallized ligand.

4.2. Ligand Preparation

We obtained the standard drug and Monacolin X structural coordinates from the PubChem database and converted them from 2D to 3D. Furthermore, all were energy-minimized using the OPLS-2005 force field [55] at pH 7 ± 2. To retain the original state, we selected the chiral centers of all ligand molecules to avoid generating stereoisomers [56].

4.3. Docking Studies

We used the Glide protocol for ligand docking in Schrödinger Suite 2026. The prepared protein active site was defined using default Glide receptor grid parameters. The ligands were docked using the XP docking protocol once the receptor grid was generated [57]. Receptor–ligand complex interaction scores, i.e., G-scores, were calculated based on the equation:

$$\text{Glide score} = 0.065 \times \text{vdW} + 0.130 \times \text{Coul} + \text{Lipo} + \text{Hbond} + \text{Metal} + \text{BuryP} + \text{RotB} + \text{Site}$$

where vdW signifies van der Waals energy, Coul represents Coulomb energy, Lipo denotes the lipophilic term derived from the hydrophobic grid potential, Hbond means the hydrogen bonding term, Metal means the metal-binding term, BuryP implies a penalty for buried polar groups, RotB infers a penalty for freezing rotatable bonds, and Site means polar interactions in the active site [58]. The molecular docking protocol was validated by redocking the co-crystallized ligands into their original binding sites in the corresponding protein crystal structure using the Glide XP docking protocol. The predicted binding pose was compared with the experimentally determined crystallographic pose by calculating the root-mean-square deviation (RMSD). The redocking RMSD values were 1.11 Å for VEGFR2, 0.27 Å for VEGFR1, 0.52 Å for Tie-2, 2.03 Å for EGFR, 0.58 Å for IGFR, 1.80 Å for NRP-1, and 0.38 Å for PDGFRα. The results for the successfully evaluated targets support the docking protocol's ability to reproduce their crystallographic ligand poses.

4.4. Molecular Dynamics Simulations

Using Desmond software, molecular dynamics simulations (MDSs) were performed on the selected receptor complexes with the lead molecules to assess the consistency of interactions. With the simple point charge (SPC) water model in an orthorhombic periodic boundary box, the complex was initially solvated (box size; distances (Å): a: 10 × b: 10 × c: 10 and angles: α: 90° × β: 90° × γ: 90°). Depending on the model's total charge, Cl− ions were added at a 0.15 M salt concentration to neutralize the system. Next, System Builder was used, with the maximum iterations set to 2000 to minimize the model. All remaining parameters were set to their default values. Finally, NPT dynamic simulations were carried out on the minimized model (isothermal–isobaric ensemble: number of particles (N), Pressure (P), and Temperature (T)) at 300 K and 1 bar, and the system was relaxed using the molecular dynamics application Desmond. Molecular dynamics simulations (a general sampling method) were performed for 50 ns. From the attained trajectory file, root-mean-square fluctuation (RMSF), root-mean-square deviation (RMSD), and H-bond interactions of the complex were evaluated. The Desmond simulation analysis also generated the interaction percentage of the complexes to annotate and describe the persistence of protein–ligand interactions during the simulations. All molecular docking and simulation studies were performed on a local workstation, a Dell Precision 3660 workstation (Dell Inc., TX, USA), equipped with a 13th Generation Intel Core i9-13900 processor (24 cores, 32 logical processors), 64 GB RAM, and an NVIDIA RTX A2000 graphics processing unit with 12 GB GPU memory. The workstation operated on Microsoft Windows 11 Pro.

5. Conclusions

Natural products and their derivatives are important sources of bioactive molecules for drug discovery, including compounds with potential anticancer and anti-angiogenic activities. In breast cancer, angiogenesis is an important biological process associated with tumor growth and progression, and targeting angiogenesis-associated molecular proteins represents a potential therapeutic strategy. In the present study, we investigated the potential activity of the Monacolin X metabolite against key molecular targets involved in the angiogenesis pathway, including VEGFR1, TIE2, EGFR, IGFR, NRP1, PGDFRα, and VEGFR2, particularly relevant to breast cancer. Counteracting or inhibiting the activity of any one of the major targets has been the approach with drugs for breast cancer treatment. Among the investigated targets, the molecular dynamics analyses provided evidence for persistent interactions between Monacolin X and VEGFR2, TIE2, PDGFRα, and EGFR. In particular, the interaction between the VEGFR2 residue CYS919 and its partner persisted throughout the simulation, with an occupancy of 68%, supporting the potential relevance of this interaction. Monacolin X also showed relatively favorable docking scores against IGFR (−9.05 kcal/mol) and PDGFRα (−7.57 kcal/mol), which were more negative than those obtained for their respective reference compounds. These findings indicate that Monacolin X may interact with multiple angiogenesis-associated targets, rather than exhibiting computational evidence restricted to VEGFR2 alone. In our previous studies, the activity of Monacolin X against VEGFR2 was reported in vitro; however, to evaluate its activity against other targets involved in angiogenesis pathways, docking and simulation studies were performed. Through these studies, the molecule's activity via binding interactions with the active site residues in targeted proteins was analyzed. Hence, Monacolin X was regarded as a VEGFR2 inhibitor. This study additionally found that Monacolin X could interact well with the additional targets TIE2, EGFR, PDGFRα, and IGFR based on the Glide score and the percentage of hydrogen bond interactions. Therefore, these hypotheses need to be validated through substantial angiogenesis-related in vitro and in vivo experiments to confirm molecular specificity. Additionally, this integrated in silico

approach can be used to investigate potential interactions between Monacolin X and other molecular targets associated with angiogenesis and cancer progression.

Author Contributions: Conceptualization, M.K.A., S.N.N., and M.B.; methodology, V.J., M.K.A., S.N.N., S.B., and M.B.; software, S.N.N. and M.B.; validation, M.B. and T.G.; formal analysis, M.K.A., S.B., J.J., C.N., and M.B., investigation and resources, M.K.A. and M.B.; data curation, V.J., S.N.N., J.J., C.N., and M.B.; writing—original draft preparation, S.N.N., S.B., and M.B.; writing—review and editing, M.K.A., S.B., J.J., C.N., and M.B.; visualization and supervision, M.K.A., M.B., and T.G.; project administration and funding acquisition, M.K.A. All authors have read and agreed to the published version of the manuscript

Funding: This research received funding from the Department of Science and Technology, Govt. of India, under the start-up research grant (young scientist) DST-SERB (SB/YS/LS-101/2014).

Institutional Review Board Statement: Not applicable.

Informed Consent Statement: Not applicable.

Data Availability Statement: The raw data are available from the corresponding author upon reasonable request.

Acknowledgments: The authors are grateful to the Centre for Molecular and Nanomedical Sciences, Sathyabama Institute of Science and Technology, Chennai for providing infrastructural facilities. The corresponding author is also grateful for the grant sanctioned by the Department of Biotechnology, Aquaculture and Marine Biotechnology, Govt. of India, under the taskforce (BT/PR11664/AAQ/3/682/2014) research grant.

Conflicts of Interest: The authors declare no conflict of interest.

References

1. Cai, Y.; Dai, F.; Ye, Y.; Qian, J. The global burden of breast cancer among women of reproductive age: Comprehensive analysis. *Sci. Rep.* **2025**, *15*, 9347. https://doi.org/10.1038/s41598-025-93883-9.
2. Ervik, M.; Laversanne, M.; Lam, F.; Colombet, M.; Ferlay, J.; Filho, A.M.; Bray, F. (2026). Global Cancer Observatory: Cancer Today (2024 estimates, version 1.0). Lyon, France: International Agency for Research on Cancer (IARC, 2026) GLOBOCAN 2024. Available online: https://gco.iarc.who.int/today/ (accessed on 01 October 2026).
3. Fu, M.; Peng, Z.; Wu, M.; Lv, D.; Li, Y.; Lyu, S. Current and future burden of breast cancer in Asia: A GLOBOCAN data analysis for 2022 and 2050. *Breast* **2025**, *79*, 103835. https://doi.org/10.1016/j.breast.2024.103835.
4. Freihat, O.; Sipos, D.; Kovacs, A. Global burden and projections of breast cancer incidence and mortality to 2050: A comprehensive analysis of GLOBOCAN data. *Front Public Health* **2025**, *13*, 1622954. https://doi.org/10.3389/fpubh.2025.1622954.
5. Yang, X.; Dong, C.; Liu, Q. Introduction and impact of the young breast cancer in China consensus. *Cancer Biol. Med.* **2025**, *23*, 8–14. https://doi.org/10.20892/j.issn.2095-3941.2025.0523.
6. Singer, C.F.; Mogg, M.; Koestler, W.; Pacher, M.; Marton, E.; Kubista, E.; Schreiber, M. Insulin-like growth factor (IGF)-I and IGF-II serum concentrations in patients with benign and malignant breast lesions: Free IGF-II is correlated with breast cancer size. *Clin. Cancer Res.* **2004**, *10*, 4003–4009. https://doi.org/10.1158/1078-0432.CCR-03-0093.
7. Wu, D.; Dong, S.; Zhou, W. Insulin-like growth factor in cancer: New perspectives (Review). *Mol. Med. Rep.* **2025**, *32*, 209. https://doi.org/10.3892/mmr.2025.13574.
8. Shyamsunder, S.; Lu, Z.; Takiar, V.; Waltz, S.E. Challenges and resistance mechanisms to EGFR targeted therapies in head and neck cancers and breast cancer: Insights into RTK dependent and independent mechanisms. *Oncotarget* **2025**, *16*, 508–530. https://doi.org/10.18632/oncotarget.28747.
9. Lee, C.; Kim, M.J.; Kumar, A.; Lee, H.W.; Yang, Y.; Kim, Y. Vascular endothelial growth factor signaling in health and disease: From molecular mechanisms to therapeutic perspectives. *Signal Transduct. Target Ther.* **2025**, *10*, 170. https://doi.org/10.1038/s41392-025-02249-0.
10. Zhang, R.; Yao, Y.; Gao, H.; Hu, X. Mechanisms of angiogenesis in tumour. *Front. Oncol.* **2024**, *14*, 1359069. https://doi.org/10.3389/fonc.2024.1359069.

11. Varanasi, S.M.; Gulani, Y.; Rachamala, H.K.; Mukhopadhyay, D.; Angom, R.S. Neuropilin-1: A Multifaceted Target for Cancer Therapy. *Curr. Oncol.* **2025**, *32*, 203. https://doi.org/10.3390/curroncol32040203.
12. Duran, C.L.; Borriello, L.; Karagiannis, G.S.; Entenberg, D.; Oktay, M.H.; Condeelis, J.S. Targeting Tie2 in the Tumor Microenvironment: From Angiogenesis to Dissemination. *Cancers* **2021**, *13*, 5730. https://doi.org/10.3390/cancers13225730.
13. Wang, P.; Mak, V.C.; Cheung, L.W. Drugging IGF-1R in cancer: New insights and emerging opportunities. *Genes Dis.* **2023**, *10*, 199–211. https://doi.org/10.1016/j.gendis.2022.03.002.
14. Kumar, S.; Chaudhri, S. Recent update on IGF-1/IGF-1R signaling axis as a promising therapeutic target for triple-negative breast cancer. *Pathol. Res. Pract.* **2024**, *263*, 155620. https://doi.org/10.1016/j.prp.2024.155620.
15. Zubair, T.; Bandyopadhyay, D. Small Molecule EGFR Inhibitors as Anti-Cancer Agents: Discovery, Mechanisms of Action, and Opportunities. *Int. J. Mol. Sci.* **2023**, *24*, 2651. https://doi.org/10.3390/ijms24032651.
16. Shetty, S.R.; Kar, T.; Das, A. Epidermal growth factor receptor mutations in breast Cancer: Therapeutic challenges and way forward. *Bioorg Chem.* **2025**, *154*, 108037. https://doi.org/10.1016/j.bioorg.2024.108037.
17. Jones, R.L.; Serrano, C.; von Mehren, M.; George, S.; Heinrich, M.C.; Kang, Y.K.; Schoffski, P.; Cassier, P.A.; Mir, O.; Chawla, S.P.; et al. Avapritinib in unresectable or metastatic PDGFRA D842V-mutant gastrointestinal stromal tumours: Long-term efficacy and safety data from the NAVIGATOR phase I trial. *Eur. J. Cancer* **2021**, *145*, 132–142. https://doi.org/10.1016/j.ejca.2020.12.008.
18. Naeem, A.; Hu, P.; Yang, M.; Zhang, J.; Liu, Y.; Zhu, W.; Zheng, Q. Natural Products as Anticancer Agents: Current Status and Future Perspectives. *Molecules* **2022**, *27*, 8367. https://doi.org/10.3390/molecules27238367.
19. Endo, A.; Hasumi, K.; Nakamura, T.; Kunishima, M.; Masuda, M. Dihydromonacolin L and Monacolin X, New Metabolites Those Inhibit Cholesterol Biosynthesis. *J. Antibiot.* **1985**, *38*, 321–327. https://doi.org/10.7164/antibiotics.38.321.
20. Nagabhishek, S.N.; Madan Kumar, A.B.S.; Balakrishnan, A.; Katakia, Y.T.; Chatterjee, S.; Nagasundaram, N. A marine sponge associated fungal metabolite monacolin X suppresses angiogenesis by down regulating VEGFR2 signaling. *RSC Adv.* **2019**, *9*, 26646–26667. https://doi.org/10.1039/c9ra05262c.
21. Jayaraman, V.; Arumugam, M.K.; Balachandran, S.; Boopathy, L.; Arumugam, S.; Srirangaramasamy, J.; Devanesan, S.; Suresh, A.; Sampath, S. Anticancer Effects of Monacolin X Against Human Liver Cancer Cell Line: Exploring the Apoptosis Using AO/EB and DCFHDA Fluorescent Staining. *Luminescence* **2025**, *40*, e70229. https://doi.org/10.1002/bio.70229.
22. Alam, T.; Hu, M.; Isaacson, R.L. The role of growth hormone in metastasis and angiogenesis of breast cancer. *Biosci. Rep.* **2026**, *46*, BSR20253516. https://doi.org/10.1042/BSR20253516.
23. Myadaraveni, P.; Palabindela, R.; Guda, R.; Banothu, D.; Kasula, M. Targeting EGFR in Breast Cancer with a Furan-Bearing NHC Precursor: Synthesis, Anticancer Activity, Molecular Docking and DFT Studies. *J. Mol. Struct.* **2026**, 1358, 145296. https://doi.org/10.1016/j.molstruc.2026.145296.
24. Shaw, P.; Dwivedi, S.K.D.; Bhattacharya, R.; Mukherjee, P.; Rao, G. VEGF signaling: Role in angiogenesis and beyond. *Biochim Biophys. Acta Rev. Cancer* **2024**, *1879*, 189079. https://doi.org/10.1016/j.bbcan.2024.189079.
25. Chen, S.; Xiang, L.; He, M.; Han, Q.; Zhang, Y.; Yang, M.; Chen, A.; Lian, J.; Li, S. Chaperone-mediated autophagy controlling VEGFR1 degradation contributes cross talk between breast cancer cells and endothelial cells triggering tumorigenesis via the VEGF-VEGFR2 axis. *Oncogene* **2025**, *44*, 4727–4746. https://doi.org/10.1038/s41388-025-03619-2.
26. Lamia, M.R.; Perri, E.; Baldassarre, G.; Pignata, S.; D'Alessio, C.; Limongello, D.; Basso-Valentina, F. Bevacizumab in ovarian cancer: Clinical data and predictive and prognostic biomarkers. *Clin. Transl. Med.* **2026**, *16*, e70591. https://doi.org/10.1002/ctm2.70591.
27. Wang, R.; Yao, S.X.; Pang, Y.W.; Huang, Y.J.; Lu, H.Y.; Pan, J.; Liu, Y.; Du, T.T.; Shi, L. Design, synthesis and biological evaluation of novel platelet-derived growth factor receptor-alpha (PDGFR-alpha) inhibitors based on 4-anilinoquinoline and 4-anilinoquinazoline scaffolds. *Eur. J. Med. Chem.* **2025**, *298*, 118015. https://doi.org/10.1016/j.ejmech.2025.118015.
28. Sun, J.; Liu, Y.; Mo, J.; Zhou, J.; Bai, X.; Gu, B.; Li, J.; Zhao, H. NCEH1 promotes breast cancer progression by regulating NRP1 and activating the TNF-alpha/NF-kappaB signalling pathway. *Cell Adh Migr.* **2026**, *20*, 2616948. https://doi.org/10.1080/19336918.2026.2616948.
29. Garg, P.; Malhotra, J.; Kulkarni, P.; Horne, D.; Salgia, R.; Singhal, S.S. Emerging Therapeutic Strategies to Overcome Drug Resistance in Cancer Cells. *Cancers* **2024**, *16*, 2478. https://doi.org/10.3390/cancers16132478.
30. Giercuszkiewicz-Hasnik, K.; Morak-Mlodawska, B.; Jelen, M. Molecularly Targeted Therapies in Oncology: Mechanisms, Resistance, and Combination Strategies. *Molecules* **2026**, *31*, 1195. https://doi.org/10.3390/molecules31071195.
31. Wu, W.; He, Y.; Zhang, C. Emerging Targeted and Multimodal Therapeutic Strategies in Breast Cancer: A Comprehensive Review. *Breast Cancer* **2026**, *18*, 575936. https://doi.org/10.2147/BCTT.S575936.

32. Zhou, J.; Jiang, X.; He, S.; Jiang, H.; Feng, F.; Liu, W.; Qu, W.; Sun, H. Rational Design of Multitarget-Directed Ligands: Strategies and Emerging Paradigms. *J. Med. Chem.* **2019**, *62*, 8881–8914. https://doi.org/10.1021/acs.jmedchem.9b00017.
33. Kabir, A.; Muth, A. Polypharmacology: The science of multi-targeting molecules. *Pharmacol. Res.* **2022**, *176*, 106055. https://doi.org/10.1016/j.phrs.2021.106055.
34. Maddeboina, K.; Yada, B.; Kumari, S.; McHale, C.; Pal, D.; Durden, D.L. Recent advances in multitarget-directed ligands via in silico drug discovery. *Drug Discov. Today* **2024**, *29*, 103904. https://doi.org/10.1016/j.drudis.2024.103904.
35. Munikumar, M.; Pradeepkiran, J.A.; Kumar, M.K.; Banapuram, S.; Bhat Edurkala, A. Comprehensive structural and functional analysis of hVEGFR1: Insights into phosphorylation, molecular interactions, and potential inhibitors through docking and dynamics simulations. *Cancer Treat. Res. Commun.* **2024**, *39*, 100795. https://doi.org/10.1016/j.ctarc.2024.100795.
36. Maji, S.; Sadhukhan, S.; Pattanayak, A.K.; Kundu, J.K. Antiangiogenic Potential of Beneficial Sterols from Parotoid Gland Secretion of Indian Common Toads (Duttaphrynus melanostictus) in the Coastal Region of the Indian Subcontinent: An In Vivo to In Silico Approach. *ACS Omega* **2025**, *10*, 10480–10492. https://doi.org/10.1021/acsomega.4c10809.
37. Saharinen, P.; Jeltsch, M.; Santoyo, M.M.; Leppänen, V.-M.; Alitalo, K. The TIE Receptor Family. In *Receptor Tyrosine Kinases: Family and Subfamilies*; Springer: Berlin/Heidelberg, Germany, 2015; pp. 743–775. https://doi.org/10.1007/978-3-319-11888-8_16.
38. Obakachi, V.A.; Govender, K.K.; Govender, P.P. A dynamic scapping workflow for RTK domains: Computational modeling of natural products as dual modulators of EGFR and VEGFR signaling in breast cancer. *Mol. Divers* **2026**, *30*, 1459–1485. https://doi.org/10.1007/s11030-025-11263-x.
39. Soni, N.; Pardasani, K.R.; Mujwar, S. Insilico analysis of dietary agents as anticancer inhibitors of insulin like growth factor 1 receptor (IGF1R). *Int. J. Pharm. Pharm. Sci.* **2015**, *7*, 191–196.
40. Marques, C.S.; Brandão, P.; Burke, A.J. Targeting Vascular Endothelial Growth Factor Receptor 2 (VEGFR-2): Latest Insights on Synthetic Strategies. *Molecules* **2024**, *29*, 5341. https://doi.org/10.3390/molecules29225341.
41. Sikuza, Y.O.K.; Basson, C.; Oberholzer, N.; Ambele, M.A. The Role of Angiogenesis in Breast Cancer and Obesity: Unravelling the Connection. *Int. J. Breast Cancer* **2026**, *20*, 2364200. https://doi.org/10.1155/ijbc/2364200.
42. Li, M.; Han, F.; Ling, S.; Su, X.; Zhao, Y.; Lv, S.; Zhang, X. Vascular Endothelial Growth Factor/Angiopoietin-2 Bispecific Antibody-Induced Vascular Normalization: From Basic Mechanisms to Therapeutic Applications in Breast Cancer. *Immun. Inflamm. Dis.* **2026**, *14*, e70408. https://doi.org/10.1002/iid3.70408.
43. Li, X.; Zhao, L.; Chen, C.; Nie, J.; Jiao, B. Can EGFR be a therapeutic target in breast cancer? *Biochim Biophys. Acta Rev. Cancer* **2022**, *1877*, 188789. https://doi.org/10.1016/j.bbcan.2022.188789.
44. Mou, J.; Li, C.; Zheng, Q.; Meng, X.; Tang, H. Research progress in tumor angiogenesis and drug resistance in breast cancer. *Cancer Biol. Med.* **2024**, *21*, 571–585. https://doi.org/10.20892/j.issn.2095-3941.2023.0515.
45. Alfaro-Arnedo, E.; López, I.P.; Piñeiro-Hermida, S.; Canalejo, M.; Gotera, C.; Sola, J.J.; Roncero, A.; Peces-Barba, G.; Ruíz-Martínez, C.; Pichel, J.G. IGF1R acts as a cancer-promoting factor in the tumor microenvironment facilitating lung metastasis implantation and progression. *Oncogene* **2022**, *41*, 3625–3639. https://doi.org/10.1038/s41388-022-02376-w.
46. Dilawar, M.; Malik, A.; Liao, J.; Shen, P.; Huang, Z.; Zhang, P.; Wang, J.; Zhang, N.; Nisar, M.F.; Chen, G. Insulin-like growth factor receptor signaling in physiology and disease. *Sig. Transduct. Target Ther.* **2026**, *11*, 375. https://doi.org/10.1038/s41392-026-02843-w.
47. Reardon, J.J.; Mossing, A.A.; Packard, R.L.; Shah, S.; Sizemore, G.M. Clinical utilities of platelet-derived growth factor signaling in breast cancer. *Pharmacol. Res.* **2026**, *231*, 108372. https://doi.org/10.1016/j.phrs.2026.108372.
48. Norman, M.H.; Liu, L.; Lee, M.; Xi, N.; Fellows, I.; D'Angelo, N.D.; Dominguez, C.; Rex, K.; Bellon, S.F.; Kim, T.S.; et al. Structure-based design of novel class II c-Met inhibitors: 1. Identification of pyrazolone-based derivatives. *J. Med. Chem.* **2012**, *55*, 1858–1867. https://doi.org/10.1021/jm201330u.
49. Tresaugues, L.; Roos, A.; Arrowsmith, C.; Berglund, H.; Bountra, C.; Collins, R.; Edwards, A.; Flodin, S.; Flores, A.; Graslund, S. Crystal structure of VEGFR1 in complex with N-(4-Chlorophenyl)-2-((pyridin-4-ylmethyl) amino) benzamide. *RCSB PDB* entry 3HNG. https://doi.org/10.2210/pdb3hng/pdb. (accessed on 01 October 2026).
50. Luke, R.W.; Ballard, P.; Buttar, D.; Campbell, L.; Curwen, J.; Emery, S.C.; Griffen, A.M.; Hassall, L.; Hayter, B.R.; Jones, C.D.; et al. Novel thienopyrimidine and thiazolopyrimidine kinase inhibitors with activity against Tie-2 in vitro and in vivo. *Bioorg Med. Chem. Lett.* **2009**, *19*, 6670–6674. https://doi.org/10.1016/j.bmcl.2009.10.001.
51. Stamos, J.; Sliwkowski, M.X.; Eigenbrot, C. Structure of the epidermal growth factor receptor kinase domain alone and in complex with a 4-anilinoquinazoline inhibitor. *J. Biol. Chem.* **2002**, *277*, 46265–46272. https://doi.org/10.1074/jbc.M207135200.
52. Degorce, S.L.; Boyd, S.; Curwen, J.O.; Ducray, R.; Halsall, C.T.; Jones, C.D.; Lach, F.; Lenz, E.M.; Pass, M.; Pass, S.; Trigwell, C. Discovery of a Potent, Selective, Orally Bioavailable, and Efficacious Novel 2-(Pyrazol-4-ylamino)-pyrimidine Inhibitor of the

Insulin-like Growth Factor-1 Receptor (IGF-1R). *J. Med. Chem.* **2016**, *59*, 4859–4866. https://doi.org/10.1021/acs.jmedchem.6b00203.
53. Jarvis, A.; Allerston, C.K.; Jia, H.; Herzog, B.; Garza-Garcia, A.; Winfield, N.; Ellard, K.; Aqil, R.; Lynch, R.; Chapman, C.; et al. Small molecule inhibitors of the neuropilin-1 vascular endothelial growth factor A (VEGF-A) interaction. *J. Med. Chem.* **2010**, *53*, 2215–2226. https://doi.org/10.1021/jm901755g.
54. Yan, X.E.; Yun, C.-H. Crystal structure of PDGFRA in Complex with WQ-C-159. *RCSB PDB* entry 5GRN. https://doi.org/10.2210/pdb5grn/pdb. (accessed on 01 October 2026).
55. Jorgensen, W.L.; Maxwell, D.S.; Tirado-Rives, J. Development and Testing of the OPLS All-Atom Force Field on Conformational Energetics and Properties of Organic Liquids. *J. Am. Chem. Soc.* **1996**, *118*, 11225–11236. https://doi.org/10.1021/ja9621760.
56. Semenova, E.V.; Belova, E.V.; Sulimov, A.V.; Sulimov, V.B. Molecular Docking of Chiral Drug Enantiomers With Different Bioactivities. *Chirality* **2024**, *36*, e23712. https://doi.org/10.1002/chir.23712.
57. Pantsar, T.; Poso, A. Binding Affinity via Docking: Fact and Fiction. *Molecules* **2018**, *23*, 1899. https://doi.org/10.3390/molecules23081899.
58. Friesner, R.A.; Banks, J.L.; Murphy, R.B.; Halgren, T.A.; Klicic, J.J.; Mainz, D.T.; Repasky, M.P.; Knoll, E.H.; Shelley, M.; Perry, J.K.; Shaw, D.E.; Francis, P.; Shenkin, P.S. Glide: A new approach for rapid, accurate docking and scoring. 1. Method and assessment of docking accuracy. *J. Med. Chem.* **2004**, *47*, 1739–1749. https://doi.org/10.1021/jm0306430.

Disclaimer/Publisher's Note: The statements, opinions and data contained in all publications are solely those of the individual author(s) and contributor(s) and not of MDPI and/or the editor(s). MDPI and/or the editor(s) disclaim responsibility for any injury to people or property resulting from any ideas, methods, instructions or products referred to in the content.